GLOBAL SEARCH FOR PLANAR AND THREE-DIMENSIONAL PERIODIC ORBITS NEAR EUROPA*

Ryan P. Russell†

A global grid search is performed to find axi- and doubly-symmetric periodic orbits in the Restricted Three Body Problem using the dimensioned parameters associated with the Jupiter-Europa system. Derived local differential correctors are applied to regions of the initial condition phase space that appear to be near solutions. The volume inside a three-dimensional initial condition mesh with billions of nodes is evaluated, and over 600,000 periodic solutions are found. Families of direct and retrograde solutions, both new and previously published, are identified and discussed. Stability is analyzed for each solution and general regions of stability are noted. Of the most promising results is the observation and characterization of a large class of stable yet highly-inclined direct orbits. Finally, all of the solutions and associated properties are archived. The resulting database is a practical reference for preliminary design of missions to Europa.

INTRODUCTION

The dynamics of the Restricted Three Body Problem (RTBP) have been studied to near exhaustion over the past two centuries. Only in recent years has the prospect of operating a spacecraft in this unique environment become a reality. In our solar system, there are potentially hundreds of three-body systems that are modeled quite well by the RTBP. As a result, engineering applications abound due to the growing appetite of the science community to send exploratory spacecraft to answer some of its most fundamental questions. Europa, in particular, has been the subject of heightened interest due to its suspected sub-surface and potentially life harboring ocean. In anticipation of future spacecraft missions to Europa, this study seeks to improve the global view of the stability properties of the six-dimensional phase space in the vicinity of Europa. Identifying and classifying periodic orbits in the Jupiter-Europa RTBP provide the basic framework for the analysis.

Periodic orbits in the Restricted Three Body Problem (RTBP) have been studied and documented by a multitude of researchers. The interested reader is referred to Broucke,[1,2] Henon,[3,4,5] Poincare,[6] and Szebehely.[7] For other studies specifically related to three-dimensional orbits, see Jeffreys,[8, 9] Goudas,[10,11] Zagouras,[12,13] Markellos,[14] and Lara.[15,16,17] A variety of techniques have been introduced to identify both specific solutions and continuous families of solutions. Under certain predictable conditions, families of solutions intersect at bifurcation points. The typical approach to scanning a particular phase space for periodic solutions is to start with a known solution (obtained by any means necessary), then parametrically continue the solution along its family in both directions until it naturally ends while noting all potential bifurcation points along the way. By this approach, a researcher can maneuver through the phase space along a web of bifurcating branches that has a structure that is a priori unknown. An alternative approach to find periodic orbits is to simply perform a grid search for each of the unknown parameters and integrate forward to check for conditions of periodicity. Then if a solution is nearby, a differential corrector can be used to target the conditions exactly. This latter brute force method is inefficient in terms of computational power, but for small enough meshes, can globally capture the full structure of most existing families without having to individually follow multiple bifurcations along a complicated set of branches. The extraordinary speed of modern computers has not only made the brute force approach practical, but for global scans it is simpler to automate and therefore is often more efficient in terms of clock time.

---

* Paper AAS05-290 for the 2005 AAS/AIAA Astrodynamics Specialist Conference in Lake Tahoe, California

† Systems Engineer, Jet Propulsion Laboratory, California Institute of Technology, 4800 Oak Grove Drive, M/S 301-140L, Pasadena, California 91109, Email: Ryan.Russell@jpl.nasa.gov. Phone: 818-393-6245, Member AAS, AIAA.

The present study applies the grid search approach on an ambitious scale to the dimensioned Jupiter-Europa system approximated by the RTBP. The differential correctors are modeled after the corrector methods used by Robin and Markellos;[14] however, the predictor step is replaced by an exhaustive grid search. The approach is based on the grid search of the planar Hill's Problem by Henon and the three-dimensional (3D) grid search of small regions in the RTBP by Kazantzis and Goudas.[18] The study is global in its attempt to identify all axi-and doubly-symmetric periodic orbits near Europa that close after crossing the *xz*-plane up to 32 and 64 times respectively. It is noted that both asymmetric orbits and orbits with no *x*-axis crossing are precluded from the search.

Families of simple periodic solutions in the context of their associated higher order resonances are illustrated in both two and three dimensions. The 3D motion clearly is related to the planar motion, and the planar motion is clearly related to one or more of the simple periodic families that exist near Europa. The analysis and discussion is based on this expected and verified phenomenon. General boundaries are identified in the phase space that separate stable or mildly unstable motion from regions of strong instability. The most noteworthy perhaps is the highly inclined stability region found in the direct case centered around altitudes of 5,500 km. The out-of-plane component is attractive for science purposes and the associated energy levels are commensurate with low-energy transfers. Finally, a variety representative orbits are illustrated, and their characteristics are documented. The complete set of solutions is archived and is of practical reference for a variety of mission design applications at Europa.

BACKGROUND

In this section, relevant background is presented including equations and appropriate derivations for the primary technical concepts associated with finding and analyzing periodic orbits.

Equations of Motion

The equations of motion for a non-thrusting spacecraft in the Jupiter-Europa Restricted Three Body Problem (RTBP) centered at Europa are given in Eq. (1) where **X** is the spacecraft state. The equations are normalized such that the radius of Europa's assumed circular orbit around the Jupiter-Europa barycenter is one distance unit (DU) and the mean motion is one radian per time unit (TU). In the rotating frame, the *x*-axis is fixed and points away from Jupiter along the Jupiter-Europa line. The *z*-axis points along Europa's angular momentum vector with respect to Jupiter, and the *y*-axis completes the right-handed coordinate system.

$$\dot{\mathbf{X}} = \mathbf{f}(\mathbf{X}, t) \tag{1}$$

where,

$$\mathbf{X} = \begin{bmatrix} x & y & z & u & v & w \end{bmatrix}^{\mathrm{T}}$$

$$\mathbf{f} = \begin{bmatrix} u \\ v \\ w \\ 2v + (x + 1 - \mu) + \kappa(x + 1) + \mu / r_E^3 \\ -2u + y + \kappa y \\ \kappa z \end{bmatrix}$$

$$\kappa = -(1-\mu)/r_J^3 - \mu/r_E^3$$

$$\mu = Gm_E/(Gm_J + Gm_E)$$

$$r_J = \sqrt{(x+1)^2 + y^2 + z^2}$$

$$r_E = \sqrt{x^2 + y^2 + z^2}$$

$$J = (x + 1 - \mu)^2 + y^2 + 2(1-\mu)/r_J + 2\mu/r_E - u^2 - v^2 - w^2 \tag{2}$$

The spacecraft distances to Europa and Jupiter are denoted as r_E and r_J respectively. The gravitational parameters for Europa and Jupiter are Gm_E and Gm_J respectively. Because the system is Hamiltonian and autonomous, an integral of motion, known as the Jacobi integral, exists of the form in Eq. (2). Table 1 gives recent estimates for the dimensioned parameters specific to the Jupiter-Europa system.[19] Thus, for converting from normalized units to km and seconds, the distance unit is 670,900 km and the derived time unit becomes 48,822.04433066813 seconds.

Table 1: Europa Parameters

Parameter	*Value*[19]
Jupiter-Europa distance [a]	6.709×10^5 km
Orbital period	3.551 day
Mean radius	1560.70 km
Europa gravitational parameter [b] (Gm_E)	3202.72 km^3/sec^2
Jupiter gravitational parameter [a,b] (Gm_J)	1.2668654×10^8 km^3/sec^2

[a] leads to Europa orbital period of 3.550 days

[b] From Eq. (1) $\mu = 2.528002607976249 \times 10^{-5}$

Variational Equations

To first order, the general time-free variation to a reference state, $\mathbf{X}_*$, at a time $t+\delta t$, is illustrated in Eq. (3) and Figure 1.

$$\delta\mathbf{X}(t+\delta t) = \tilde{\delta}\mathbf{X}(t) + \dot{\mathbf{X}}_*(t)\delta t \tag{3}$$

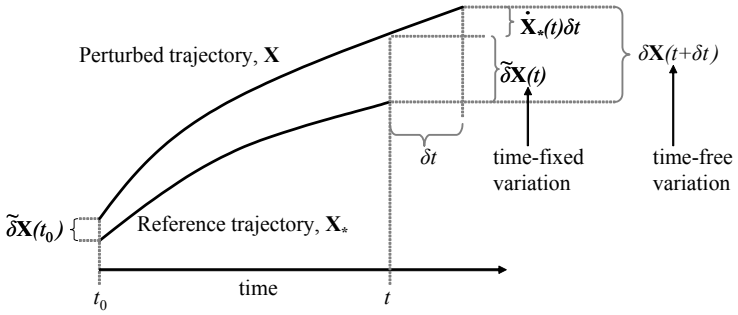

Figure 1: Variations

The time-fixed variation at a given time is obtained by mapping an initial perturbation forward using the state transition matrix, $\mathbf{\Phi}(t,t_0)$, also known as the fundamental matrix.[1]

$$\tilde{\delta}\mathbf{X}(t) = \mathbf{\Phi}(t,t_0)\tilde{\delta}\mathbf{X}(t_0) \tag{4}$$

Equation (4) is derived by substituting $\mathbf{X} = \mathbf{X}_* + \tilde{\delta}\mathbf{X}$ into Eq. (1) and expanding the right-hand side into a Taylor series in $\mathbf{X}$ centered about $\mathbf{X}_*$. The resulting first order linear differential equation is:

$$\tilde{\delta}\dot{\mathbf{X}}(t) = \left(\partial\mathbf{f}/\partial\mathbf{X}\right)\Big|_* \tilde{\delta}\mathbf{X}(t) \tag{5}$$

A solution is sought of the form given in Eq. (4). Comparing Eq. (5) to a time derivative of Eq. (4) yields:

$$\dot{\mathbf{\Phi}}(t,t_0)\tilde{\delta}\mathbf{X}(t_0) = \left(\partial\mathbf{f}/\partial\mathbf{X}\right)\Big|_* \tilde{\delta}\mathbf{X}(t) = \left(\partial\mathbf{f}/\partial\mathbf{X}\right)\Big|_* \mathbf{\Phi}(t,t_0)\tilde{\delta}\mathbf{X}(t_0)$$

Thus, for an arbitrary $\tilde{\delta}\mathbf{X}(t_0)$, the state transition matrix is obtained by integrating Eq. (6) along the reference trajectory.

$$\dot{\mathbf{\Phi}}(t,t_0) = \left(\partial \mathbf{f}/\partial \mathbf{X}\right)\Big|_* \mathbf{\Phi}(t,t_0) \qquad (6)$$
$$\mathbf{\Phi}(t_0,t_0) = \mathbf{I}$$

The partial derivative in Eq. (6) is known as the Jacobian and for the RTBP is given by:

$$\left(\partial \mathbf{f}/\partial \mathbf{X}\right) = \begin{bmatrix} \mathbf{0}_{3x3} & \mathbf{I}_{3x3} \\ \mathbf{G}_{3x3} & \mathbf{H}_{3x3} \end{bmatrix} \quad \mathbf{H} = \begin{bmatrix} 0 & 2 & 0 \\ -2 & 0 & 0 \\ 0 & 0 & 0 \end{bmatrix}$$

$$G_{1,1} = (1-\mu)\left[2(x+1)^2 - y^2 - z^2\right]/r_J^5 + \mu\left(2x^2 - y^2 - z^2\right)/r_E^5 + 1$$
$$G_{2,2} = (1-\mu)\left[2y^2 - (x+1)^2 - z^2\right]/r_J^5 + \mu\left(2y^2 - x^2 - z^2\right)/r_E^5 + 1$$
$$G_{3,3} = (1-\mu)\left[2z^2 - (x+1)^2 - y^2\right]/r_J^5 + \mu\left(2z^2 - x^2 - y^2\right)/r_E^5 + 1$$
$$G_{1,2} = G_{2,1} = 3(1-\mu)(x+1)\,y/r_J^5 + 3\,\mu xy/r_E^5$$
$$G_{1,3} = G_{3,1} = 3(1-\mu)(x+1)\,z/r_J^5 + 3\,\mu xz/r_E^5$$
$$G_{2,3} = G_{3,2} = 3(1-\mu)\,yz/r_J^5 + 3\,\mu yz/r_E^5$$

Substituting Eq. (4) into (3), Eq. (7) is the general first-order expression for obtaining the state perturbations at a given time, *t,* due to small perturbations in *t* and the initial state.

$$\delta \mathbf{X}(t+\delta t) = \mathbf{\Phi}(t,t_0)\tilde{\delta}\mathbf{X}(t_0) + \dot{\mathbf{X}}_*(t)\delta t \qquad (7)$$

Equation (7) provides the derivatives of a final state with respect to an initial state and will be used to differentially correct initial conditions to find periodic orbits. Additionally, the state transition matrix will play an important role in determining the stability of a given periodic orbit. These applications will be addressed further in the following two sections.

Stability

The state transition matrix evaluated after a full period, $t=T$, of a periodic orbit is referred to as the Monodromy matrix.[20] This matrix provides a linear mapping for small initial state perturbations across one full period. By definition, an eigenvalue, λ (real or complex), of the Monodromy matrix is a scalar proportionality factor that satisfies the relation:

$$\mathbf{\Phi}(T,t_0)\boldsymbol{\xi} = \lambda\boldsymbol{\xi} \qquad (8)$$

Thus for an eigenvalue with a magnitude greater than unity, perturbations in the eigen-direction, $\boldsymbol{\xi}$, will grow after one period, and the orbit is unstable in this direction. Because of the symplectic[21] nature of the state transition matrix, Broucke, among others, has shown that the eigenvalues of the Monodromy matrix occur in reciprocal pairs.[1] Furthermore, for the RTBP, one of the eigenvalues will be unity due to the existence of the Jacobi integral stated in Eq.(2).[1,20] Thus, the eigenvalues of the Monodromy matrix for the three-dimensional RTBP will have the form $\{\lambda_1,\ 1/\lambda_1,\ \lambda_2,\ 1/\lambda_2,\ 1,\ 1\}$. Therefore, if an eigen-direction exist that leads to a contraction, then there is also an accompanying eigen-direction that leads to an expansion. Thus, all eigenvalues must have a magnitude of 1 in order to avoid expansions in any direction.

The characteristic equation of the Monodromy matrix is written as,

$$\det\left[\mathbf{\Phi}(T,t_0) - \lambda\mathbf{I}\right] = (\lambda-1)^2\left[(\lambda-\lambda_1)(\lambda-1/\lambda_1)(\lambda-\lambda_2)(\lambda-1/\lambda_2)\right] = 0 \qquad (9)$$

Eq. (9) can be rewritten to define two sets of commonly used stability parameters (a_1,a_2) and (k_1,k_2).[1, 17]

$$(\lambda-1)^2\left(\lambda^4 + a_1\lambda^3 + a_2\lambda^2 + a_1\lambda + 1\right) = (\lambda-1)^2\left(\lambda^2 - k_1\lambda + 1\right)\left(\lambda^2 - k_2\lambda + 1\right) = 0 \qquad (10)$$

Note that a_i is always real because the quartic in Eq. (10) comes directly from the determinant of a real matrix, while factoring it into the two quadratics may require k_i to be complex.

The roots of Eq. (10) lead to seven categories for eigenvalue classification, each corresponding to a specific region in the (a_1,a_2) plane.[1] Only one region (with a rather complicated shape) corresponds to linear stability, i.e. ensures that λ_1 and λ_2 are on the unit circle. Stated in terms of the (k_1,k_2) plane, the region of stability is the much simpler shape defined by the rectangle $|k_i| \le 2$, with the requirement that k_i is real.

The current study seeks a wide range of solutions, not limited to orbits with non-complex values of k_i. Furthermore, due to the complicated shape of the stability region in the always real (a_1,a_2) plane, it is it difficult to comparatively measure how far a particular unstable orbit is from the stability boundary. Thus, for unstable orbits, a single, real, scalar index of *in*stability is proposed and defined in Eq. (11).

$$\rho = \max\left\{\left|\lambda_1\right|, \left|1/\lambda_1\right|, \left|\lambda_2\right|, \left|1/\lambda_2\right|\right\} \tag{11}$$

Stable orbits will have a ρ value of 1, and because each eigenvalue shares a reciprocal pair, 1 is the lower bound. Note that for a stable orbit, it is still interesting to evaluate the k stability indices ($k_i=\lambda_i+1/\lambda_i$) because they are always real and have a range $-2 \le k_i \le 2$. Certain critical values of k_i lead to potential bifurcations, or points of intersection between two or more families of periodic orbits. A great deal of references discuss these bifurcations and the associated stability indices.[1,5,7,13,14] The search method employed in this study is a global grid search and does not depend on bifurcations; therefore, the indices discussed in this section are evaluated for each of the identified solutions only for analysis and potential future use.

From comparing coefficients in Eqs. (9) and (10), the following relations are found:

$$\left.\begin{matrix} k_1 \\ k_2 \end{matrix}\right\} = \frac{a_1 \pm \sqrt{a_1^2 - 4a_2 + 8}}{2} \qquad \left.\begin{matrix} \lambda_i \\ 1/\lambda_i \end{matrix}\right\} = \frac{k_i \pm \sqrt{k_i^2 - 4}}{2} \tag{12}$$

Eq. (13) gives a fast method for calculating a_i and is derived in Ref. 10 and restated in Refs 12 and 13. (Note, the equations presented are correct, but there is an error in Ref 10 regarding the stability when k_i is complex.[3])

$$\begin{aligned} a_1 &= 2 - \text{trace}\left[\boldsymbol{\Phi}(T,t_0)\right] \\ a_2 &= \left\{a_1^2 + 2 - \text{trace}\left[\boldsymbol{\Phi}(T,t_0)\boldsymbol{\Phi}(T,t_0)\right]\right\}/2 \end{aligned} \tag{13}$$

Thus, a fast method for obtaining the eigenvalues and all of the associated stability and instability indices of the Monodromy matrix is found from Eqs. (11)-(13).

Symmetries

If the variable transformation $\{t=-t, y=-y\}$ is applied, then the state and associated derivatives become:

$$\begin{aligned} \left[x \quad y \quad z \quad u \quad v \quad w\right]^{\mathrm{T}} &\rightarrow \left[x \quad -y \quad z \quad -u \quad v \quad -w\right]^{\mathrm{T}} \\ \left[\dot{x} \quad \dot{y} \quad \dot{z} \quad \dot{u} \quad \dot{v} \quad \dot{w}\right]^{\mathrm{T}} &\rightarrow \left[-\dot{x} \quad \dot{y} \quad -\dot{z} \quad \dot{u} \quad -\dot{v} \quad \dot{w}\right]^{\mathrm{T}} \end{aligned}$$

Plugging the derivative transformations into the left side of Eq. (1) and state transformations into the right side, the resulting equations are identical to those prior to the transformation. The RTBP equations of motion are therefore invariant under the transformation $\{t=-t, y=-y\}$. The implications are as follows: If an arbitrary initial condition (x_0, y_0, z_0) is integrated forward in time, the resulting trajectory will be a mirror-image (with respect to the xz-plane) of the trajectory integrated backwards in time starting from the initial conditions $(x_0, -y_0, z_0)$. This is illustrated in Figure 2a.

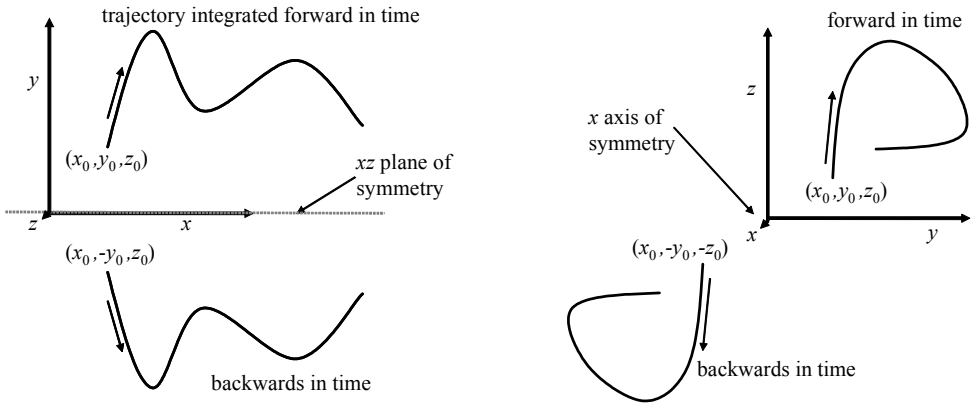

a) symmetry with the *xz* plane (mirror-image) **b) symmetry with *x* axis (180° rotation)**

Figure 2: Symmetry in the RTBP

Thus, if a trajectory has an initial position on the *xz*-plane and an initial velocity perpendicular to the *xz*-plane, then the backwards integrated mirror-image motion will have a continuous position and velocity with the forward integrated motion at the *xz*-plane crossing. Therefore, instead of two mirror-image trajectories with discontinuities [as seen in Figure 2(a)], it can be considered as one continuous trajectory that exhibits symmetry centered around a perpendicular crossing of the property of the *xz*-plane. If, in addition, the trajectory ends in a perpendicular crossing, then this state also will exhibit the symmetric motion when integrated forwards and backwards with no discontinuities. Therefore, the trajectory is closed, and the motion is periodic. It follows then, if a RTBP trajectory is found with two perpendicular crossings of the *xz*-plane separated by a time, $T/2$, then the trajectory is periodic with a period, T.

The equations of motion can also be easily shown to be invariant under the transformation $\{t=-t, y=-y, z=-z\}$. If an arbitrary initial condition (x_0, y_0, z_0) is integrated forward in time, the resulting trajectory will be a 180° rotation (of the *x*-axis) of the trajectory integrated backwards in time starting from the initial conditions $(x_0, -y_0, -z_0)$. This is illustrated in Figure 2b. It follows then, from a similar argument to that above, if a RTBP trajectory is found with two perpendicular crossings of the *x*-axis separated by a time, $T/2$, then the trajectory is periodic with a period, T. This type of simply-symmetric orbit is referred to as an axi-symmetric periodic orbit.[12, 14]

The most obvious symmetry of the RTBP is the symmetry with respect to the *xy*-plane. In this case the equations of motion are invariant under the simple transformation $\{z=-z\}$ with no reversal of time. Thus, if an arbitrary initial condition (x_0, y_0, z_0) is integrated forward, the resulting trajectory will be a mirror image (with respect to the *xy*-plane) of the trajectory integrated forward starting from the initial conditions $(x_0, y_0, -z_0)$.

A doubly-symmetric orbit is one that enjoys the *xz*-planar symmetry and *x*-axis symmetry.[8,9,10,18] Note, that it also exhibits the *xy*-planar symmetry, but there is no mention of it being called a triply-symmetric orbit in the literature. If an orbit begins on and is perpendicular to the *x*-axis with initial conditions $(x_0, 0, 0, 0, v_0, w_0)$ and ends perpendicular to the *xz*-plane with a state $(x_{T/4}, 0, z_{T/4}, 0, v_{T/4}, 0)$ and $t=T/4$, then by the *xz*-plane symmetry, the orbit will trace a mirror image and re-encounter the *x*-axis with a state $(x_0, 0, 0, 0, v_0, -w_0)$ and $t=T/2$. Then, by the *xy*-plane symmetry, the orbit will re-trace the full trajectory with $z=-z$ and re-encounter the *x*-axis with the original state $(x_0, 0, 0, 0, v_0, w_0)$ and $t=T$. It is also axi-symmetric because it has two perpendicular crossings of the *x*-axis.

From the discussion above, it is only necessary to integrate half of the full period for an axi-symmetric orbit and one-quarter period for the doubly-symmetric orbit. However, the Monodromy matrix, or the state transition matrix evaluated over one full period, is needed to evaluate stability. Equation (14) gives a fast method to calculate the Monodromy matrix for the axi- and doubly-symmetric orbits that start on the *x*-axis

without having to integrate the full period, where **L** and **K** are 6 x 6 identity matrices with the exception of $L_{1,1}$= $L_{4,4}$= $L_{6,6}$= $K_{1,1}$= $K_{3,3}$= $K_{5,5}$=-1. For details, see Ref. 14.

$$\begin{aligned}\mathbf{\Phi}(T,t_0)_{\text{axi}} &= \mathbf{L}\mathbf{\Phi}^{-1}(T/2,t_0)\mathbf{L}\mathbf{\Phi}(T/2,t_0)\\ \mathbf{\Phi}(T,t_0)_{\text{doubly}} &= \left[\mathbf{L}\mathbf{\Phi}^{-1}(T/4,t_0)\mathbf{K}\mathbf{\Phi}(T/4,t_0)\right]^2\end{aligned} \tag{14}$$

Differential Correctors

In this section, local differential correctors are derived in order to target axi- and doubly-symmetric orbits based on their respective conditions for periodicity and Eq. (7). The equations are based on the first order terms in a linearization of a highly nonlinear system; therefore, the initial orbit must be in the neighborhood of a solution, and typically several iterations are required for convergence.[22]

Axi-symmetric

An orbit with two perpendicular crossings of the *x*-axis is axi-symmetric. One set of associated conditions for periodicity is given as,

$$\{y_0 = z_0 = u_0 = 0\} \text{ and } \{y_{T/2} = z_{T/2} = u_{T/2} = 0\} \tag{15}$$

The first three conditions of Eq. (15) are automatically satisfied by starting all orbits on and perpendicular to the *x*-axis. Thus, the search parameters become $\{x_0, v_0, w_0, T/2\}$. It is desired to adjust these four parameters such that the final three conditions are met. Given a reference orbit that is near axi-symmetric, the search perturbations to the initial state to be used in Eq. (7) become

$$\tilde{\delta}\mathbf{X}_0 = \begin{bmatrix}\tilde{\delta}x_0 & 0 & 0 & 0 & \tilde{\delta}v_0 & \tilde{\delta}w_0\end{bmatrix}^{\mathsf{T}} \tag{16}$$

Inserting Eq. (16) into Eq. (7), the perturbations of interest at the final state become

$$\begin{bmatrix}\delta y_{T/2}\\ \delta z_{T/2}\\ \delta u_{T/2}\end{bmatrix} = \begin{bmatrix}\Phi_{yx} & \Phi_{yv} & \Phi_{yw}\\ \Phi_{zx} & \Phi_{zv} & \Phi_{zw}\\ \Phi_{ux} & \Phi_{uv} & \Phi_{uw}\end{bmatrix}_{T/2}\begin{bmatrix}\tilde{\delta}x_0\\ \tilde{\delta}v_0\\ \tilde{\delta}w_0\end{bmatrix} + \begin{bmatrix}\dot{y}_{T/2}\\ \dot{z}_{T/2}\\ \dot{u}_{T/2}\end{bmatrix}\delta t \tag{17}$$

The $y_{T/2}$=0 periodicity condition of Eq. (15) can be automatically enforced by terminating the state propagation after the spacecraft has exactly *N* crossings of the *xz*-plane. The reference orbit, then, ends with $y_{T/2}$=0 exactly. Of course the corrected orbit should also end on the *xz*-plane, and thus $\delta y_{T/2}$ is set to zero. Solving for δt in the top row of Eq. (17) gives,

$$\delta t = \left(-1/\dot{y}_{T/2}\right)\left(\Phi_{yx}\tilde{\delta}x_0 + \Phi_{yv}\tilde{\delta}v_0 + \Phi_{yw}\tilde{\delta}w_0\right) \tag{18}$$

Inserting Eq. (18) into the remaining rows of Eq. (17) gives

$$\begin{bmatrix}\delta z_{T/2}\\ \delta u_{T/2}\end{bmatrix} = \left[\begin{pmatrix}\Phi_{zx} & \Phi_{zv} & \Phi_{zw}\\ \Phi_{ux} & \Phi_{uv} & \Phi_{uw}\end{pmatrix} - \frac{1}{\dot{y}}\begin{pmatrix}\dot{z}\\ \dot{u}\end{pmatrix}\begin{pmatrix}\Phi_{yx} & \Phi_{yv} & \Phi_{yw}\end{pmatrix}\right]_{T/2}\begin{bmatrix}\tilde{\delta}x_0\\ \tilde{\delta}v_0\\ \tilde{\delta}w_0\end{bmatrix} \tag{19}$$

Eq. (19) is under-constrained because there are three unknowns and two constraints. Thus, any of the three initial perturbations to *x*, *v*, or *w* can be fixed to zero and a unique expression is easily obtained for the other two. For example, if a solution is sought with the same *x*-axis crossing as the reference orbit, then $\tilde{\delta}x_0 = 0$ and

$$\begin{bmatrix}\delta z_{T/2}\\ \delta u_{T/2}\end{bmatrix} = \left[\begin{pmatrix}\Phi_{zv} & \Phi_{zw}\\ \Phi_{uv} & \Phi_{uw}\end{pmatrix} - \frac{1}{\dot{y}}\begin{pmatrix}\dot{z}\\ \dot{u}\end{pmatrix}\begin{pmatrix}\Phi_{yv} & \Phi_{yw}\end{pmatrix}\right]_{T/2}\begin{bmatrix}\tilde{\delta}v_0\\ \tilde{\delta}w_0\end{bmatrix}$$

The reference orbit ends with some near-zero values for $z_{T/2}$ and $u_{T/2}$. In order to drive these to zero for the corrected orbit, $\delta z_{T/2}$ and $\delta u_{T/2}$ are set to $-z_{T/2}$ and $-u_{T/2}$ respectively. Solving for the unknowns gives the final form for the differential corrector used in this study when searching for axi-symmetric orbits. Note that Eq. (20) is valid given a near-axi-symmetric reference trajectory is provided. Also, remember that *T*/2 is chosen independently for both the reference trajectory and the corrected trajectory such that $y_{T/2}$ is zero to machine

precision. The matrix in Eq. (20) is always invertible because the columns of the state transition matrix are simply a scaled set of the linearly independent general solutions to Eq. (5).

$$\begin{bmatrix} \tilde{\delta}v_0 \\ \tilde{\delta}w_0 \end{bmatrix} = \begin{bmatrix} \Phi_{zv} - \dot{z}\Phi_{yv}/\dot{y} & \Phi_{zw} - \dot{z}\Phi_{yw}/\dot{y} \\ \Phi_{uv} - \dot{u}\Phi_{yv}/\dot{y} & \Phi_{uw} - \dot{u}\Phi_{yw}/\dot{y} \end{bmatrix}_{T/2}^{-1} \begin{bmatrix} -z_{T/2} \\ -u_{T/2} \end{bmatrix} \tag{20}$$

Doubly-Symmetric

An orbit with one perpendicular crossing of the *x*-axis and one perpendicular crossing of the *xz*-plane is doubly-symmetric. One set of associated conditions for periodicity is given as

$$\{ y_0 = z_0 = u_0 = 0 \} \text{ and } \{ y_{T/4} = u_{T/4} = w_{T/4} = 0 \} \tag{21}$$

Note, the initial three conditions from Eq. (21) are identical to those in Eq. (15). Thus, for a doubly-symmetric, the search perturbations to the initial state to be used in Eq. (7) are identical to those in Eq. (16). The final three conditions in Eq. (21) are the same as those in Eq. (15) with the exception that a doubly-symmetric orbit targets $z_{T/4}$=0 instead of $w_{T/4}$=0. By a similar procedure as shown for the axi-symmetric orbit, Eq. (22) gives the final form for the differential corrector used in this study when searching for doubly-symmetric orbits. Note that Eq. (22) is valid given a near-doubly-symmetric reference trajectory is provided. As in the case for the axi-symmetric orbit, the resulting corrected trajectory will have the same initial x_0 as the reference. And again, T/4 is chosen independently for both the reference trajectory and the corrected trajectory such that $y_{T/4}$ is zero to machine precision.

$$\begin{bmatrix} \tilde{\delta}v_0 \\ \tilde{\delta}w_0 \end{bmatrix} = \begin{bmatrix} \Phi_{uv} - \dot{u}\Phi_{yv}/\dot{y} & \Phi_{uw} - \dot{u}\Phi_{yw}/\dot{y} \\ \Phi_{wv} - \dot{w}\Phi_{yv}/\dot{y} & \Phi_{ww} - \dot{w}\Phi_{yw}/\dot{y} \end{bmatrix}_{T/4}^{-1} \begin{bmatrix} -u_{T/4} \\ -w_{T/4} \end{bmatrix} \tag{22}$$

Planar

If motion is restricted to the *xy*-plane, Eq. (20) can be reduced to a one-dimensional expression given in Eq. (23). Henon calls this N periodic symmetry, where a solution has N-1 intermediate non-perpendicular crossings of the *x*-axis. Equation (23) can also be derived from Eq. (22) because, in the planar case, a perpendicular crossing of the x-axis is also a perpendicular crossing of the *xz*-plane. Note that the time between perpendicular crossings is T/2 rather than T/4 because the planar orbit does not require the period doubling associated with the *xy*-plane symmetry of the three-dimensional doubly-symmetric orbit.

$$\tilde{\delta}v_0 = \frac{-u_{T/2}}{\left(\Phi_{uv} - \dot{u}\Phi_{yv}/\dot{y}\right)_{T/2}} \tag{23}$$

GLOBAL GRID SEARCH

As discussed above, axi- and doubly-symmetric periodic orbits can be initiated on and perpendicular to the *x*-axis. Thus, an exhaustive grid search over the four dimensional space $\{x_0, v_0, w_0, T\}$ is sufficient to find all axi- and doubly-symmetric periodic orbits. The search parameter T, the orbit period, can be replaced by the integer-valued N because the terminal conditions for both types of orbits occur at *xz*-plane crossings. Thus, for a given set of $\{x_0, v_0, w_0\}$, the trajectory is integrated forward with $y_0 = z_0 = u_0 = 0$ and is terminated on the N^{th} crossing of the *xz*-plane with a final time, t_f. If the final velocity is near perpendicular to the *x*-axis, then Eq. (20) is applied and the process is iterated until convergence if possible. If a solution is found, it is deemed an axi-symmetric N periodic orbit with $T = 2t_f$. If the final velocity is near perpendicular to the *xz*-plane, then Eq. (22) is applied and the process is iterated until convergence, if possible. If a solution is found, it is deemed a doubly-symmetric N periodic orbit with $T = 4t_f$. Figure 3 shows a sample trajectory with the labeled search parameters $\{x_0, v_0, w_0, N\}$.

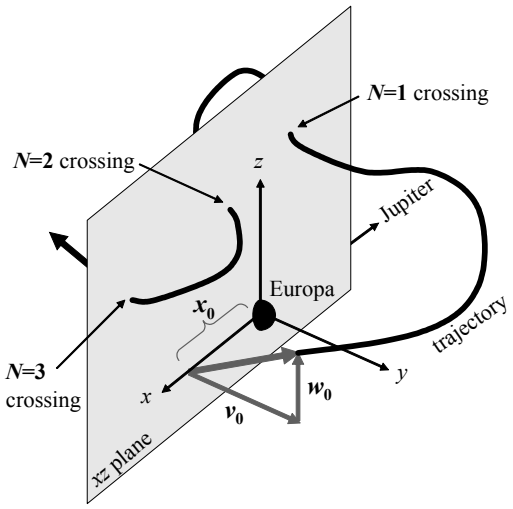

Figure 3: Sample trajectory and associated search parameters: x_0, v_0, w_0, and N

To be consistent with Henon,[3] x_0 is allowed to be positive or negative while v_0 and w_0 are restricted to be positive only. Note that any solution with positive w_0 in the RTBP also exists with negative w_0 due to the xy-plane symmetry. Also note, for every perpendicular x-axis crossing with a positive v, there is a reciprocal x-axis crossing with a negative v. Thus, duplicate orbits are avoided by seeking only positive values for v_0. Trajectories with positive x_0 move initially in a direct motion with respect to Europa, and trajectories with negative x_0 are initially retrograde.

It is noted that the search space is limited to trajectories with x-axis crossings. Therefore, the class of orbits that exhibit the xz-plane symmetry but not the x-axis symmetry will not be found with this search. The halo family[23] is a notable example that is precluded from the present search. For examples of the halo family for the Jupiter-Europa system see Ref. 17.

For a given x_0, the $\{v_0, w_0\}$ space is searched for N=1→N_{max}, and Eq. (20), (22), or (23) is applied to find axi-symmetric, doubly-symmetric, or planar solutions respectively. In general, the solutions appear as points in the v_0w_0 plane. This process is repeated for a sufficient number of x_0 values, and when all the solutions are plotted in the three-dimensional $\{x_0, v_0, w_0\}$ space, families of solutions appear as two-dimensional lines. For a slice of constant x_0, Figure 4 illustrates the interior mesh points in the v_0w_0 plane and example solutions.

The differential correctors require multiple shooting of the integration of the six-state plus 36 variational equations. Computationally they are roughly two orders of magnitude more expensive than simply integrating a six-state just once. For a sufficiently fine mesh then, it is neither efficient nor practical to apply each of the differential correctors at every node. Ideally, each converged solution should only require one implementation of a differential corrector. For example, from Figure 4, all 9 nodes might lead to final states that are near the periodicity conditions associated with the indicated solution; however, it would be inefficient to apply the differential corrector each time only to find the same solution.

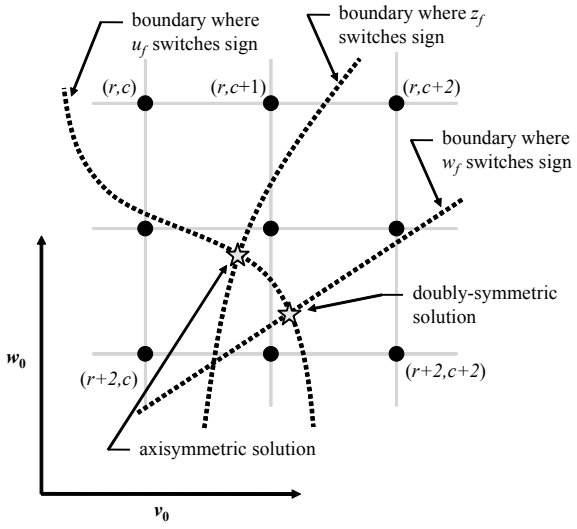

Figure 4: Interior mesh points for the v_0w_0 grid at a given $\mathbf{x_0}$

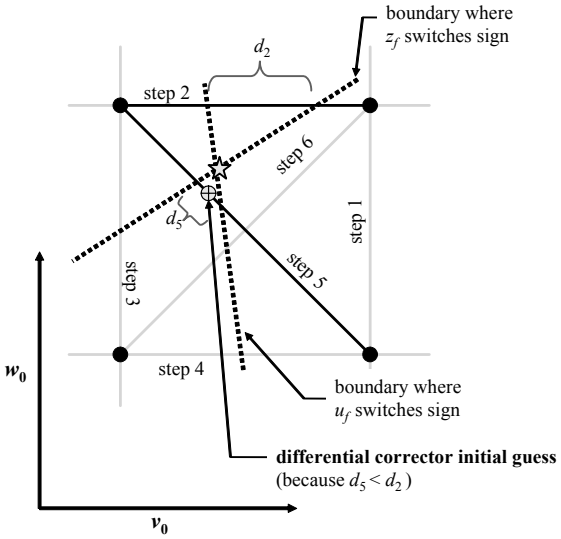

Figure 5: Near-solution criteria and initial guess for differential corrector

To reduce duplicate solutions, the differential corrector is only called when a defined criteria is met indicating a solution is nearby. The chosen criteria is based on sign changes for the target conditions.[3,18] As illustrated in Figure 4, an axi-symmetric solution generally exists at the intersection of two lines where the signs of z_f and u_f change, and a doubly-symmetric solution generally exists at the intersection of two lines where the signs of u_f and w_f change. The term generally is used because it is possible, though unlikely, that a solution exists without such a boundary. For instance, the u_f corresponding to a solution may have a zero value with no sign change boundary because it is a local extremum. If the boundary does exist however, a solution is in the vicinity if a step in any direction on the grid leads to sign changes in both periodicity conditions. For example, if the step is taken from node (r+1,c) to node (r+1,c+1), this indicates the presence of a nearby axi-symmetric solution because both z_f and u_f change signs. A doubly-symmetric solution is detected if stepping vertically from node (r+2,c+1) to node (r+1,c+1) because both w_f and u_f change signs. Note, in this example, no single step in the vertical direction detects the axi-symmetric solution whereas no single step in the horizontal direction detects the doubly-symmetric solution. Thus for completeness, multiple step directions should be considered when looking for a dual sign change. It is noted that the mesh must be sufficiently fine such that two unique boundary lines for the same variable are never crossed in one step, otherwise, a change in sign for this variable will go undetected.

For fine meshes, the sign change boundaries become lines and the intersections become an 'X' as illustrated in Figure 5. The six step-directions are introduced and all six are evaluated for a dual crossing. If a solution exists inside the four nodes and if the boundaries are in fact lines, then the 'X' can be oriented such that as few as one or as many as four step directions have dual crossings. In the example shown, steps 2 and 5 meet the criteria. The normalized distances, d_2 and d_5, are evaluated via interpolation assuming u_f and z_f behave linearly from node to node. The initial guess for the differential corrector is then placed at the midpoint between the two intersections on the step associated with the smallest distance.

```
FOR  x0 = x0min to x0max by dx0 (increment ix)
   FOR  w0 = w0min to w0max by dw0 (increment iw)
      FOR  v0 = v0min  to v0max by dv0 (increment iv)
         X = X0  (y0 = z0 = u0 =0)
         FOR N=1 to Nmax by 1
            Propagate X to the next crossing of xz-plane (or impact/escape Europa)
            IF [no impact or escape]
               Store zf ,uf ,wf in Row(iv,1:3)
               IF [w0=0 and iv>1]
                  Planar=False
                  IF [sign change in uf]
                     Use Row to interpolate to zero uf crossing (record x0 and vp0)
                     Planar=True
               ELSEIF [iv>1 and iw>1]
                  FOR Step=1 to 6 by 1
                     Axi-symmetric=False, DoublySymmetric=False
                     IF [sign changes in uf and zf along Step direction] (Use Row and LastRow)
                        Interpolate to find zero crossings on the Step line
                        Calculate axi-symmetric dStep from Figure 5
                        Axi-symmetric=True
                     IF [sign changes in uf and wf along Step direction] (Use Row and LastRow)
                        Interpolate to find zero crossings on the Step line
                        Calculate doubly-symmetric dStep from Figure 5
                        DoublySymmetric= True
                  END Step loop
               IF [Axi-symmetric]
                  Evaluate best va0, and wa0 based on min(axi-symmetric dStep)
                  Send x0, va0, and wa0 as initial guess to axi-symmetric differential corrector
               IF [DoublySymmetric]
                  Evaluate best vd0 and wd0 based on min(doubly-symmetric dStep)
                  Send x0, vd0, and wd0 as initial guess to doubly-symmetric differential corrector
               IF [Planar]
                  Send x0 and vp0 as initial guess planar differential corrector
               Record any differential corrector solutions
               Check for repeated solutions and false classifications (N and symmetry)
               Evaluate the stability and other characteristics (N, T,…) of final solution
         END N loop
      END v0 loop
      LastRow=Row
   END w0 loop
END x0 loop
```

Figure 6: Grid search algorithm

The implementation effort for the described process is significantly reduced by simplifying the interpolation scheme or removing it entirely and only giving node values as initial guesses. However, because the 2D grid search must be repeated for sufficiently spaced slices of constant x_0, even with the extraordinary speed of modern computers, there is a practical limitation in the fineness of the mesh resolution. Thus, for a large-scale 3D global search, it remains beneficial to wisely select a near-solution criteria along with an initial guess interpolation scheme. It is noted that a variety of other interpolation strategies and near-solution criteria are possible. The described approach is generally found to be an appropriate balance between computational effort and search completeness. The algorithm is given in Figure 6.

The planar and the 3D cases are evaluated independently because entire families of planar solutions are known to exist and the reduced dimension affords a much finer mesh. In both cases, the algorithm is applied first with a course mesh with liberal values for ranges on the search space $\{ x_0,\ v_0,\ w_0,\ N \}$ to determine appropriate mesh sizes and ranges for later more refined searches. Table 2 presents the associated mesh parameters with each of the final four search regions.

All trajectories are integrated with a variable step Runge-Kutta 7(8) routine that is modified to allow for a general stopping condition, i.e. at *xz*-plane crossings. For the initial shooting, the error tolerance is set such that the Jacobi constant remains fixed up to 8 significant digits. In the differential correctors, the error accuracy is increased to maintain approximately 13 digits in the Jacobi constant, and the convergence criteria, or the norm of periodicity constrains, must be met to a tolerance of 1E-10.

The algorithm is robust in detecting and honing in on solutions, especially for lower values of N. As N is increased, the number of existing solutions increases in a nonlinear fashion. Accordingly, the resolution of the mesh must also be refined in order to detect most of the solutions on a given family. For the final run, N_{max} is chosen to be 16. This is equivalent to a maximum of 32 and 64 xz-plane crossings respectively for the full period axi- and doubly-symmetric solution. Remember the axi- and doubly-symmetric solutions are found after only half and a quarter of their full periods respectively. For the given mesh, the algorithm captures enough of the higher resonant solutions to visualize families and trends of stability.

Table 2: Global search regions and parameters for N_{max} =16

Search Region	x_{0min}	x_{0max}	# x_0 [a]	v_{0min} (km/s)	v_{0max} (km/s)	# v_0 [a]	w_{0min} (km/s)	w_{0max} (km/s)	# w_0 [a]
Planar Retrograde	-150,000 km	surface [b]	2,000	0.0	7.0	80,000	0.0	0.0	1
Planar Direct	surface [b]	*L*2[c]	1,000	0.0	2.0	40,000	0.0	0.0	1
3D Retrograde I	-150,000 km	-50,000 km	2,000	2.0	7.0	2,500	0.0001	1.5	750
3D Retrograde II	-50,000 km	Surface [b]	3,000	0.0001	2.5	1,250	0.0001	3.0	1,500
3D Direct	surface [b]	*L*2[c]	1,000	0.0001	2.0	1,000	0.0001	2.0	1,000

[a] number of equally spaced values
[b] Europa radius defined in Table 1
[c] *L*2: far-side of Europa collinear libration point, x_{L2} = 13,744 km, *L*1: interior collinear libration point, x_{L1} = -13,559 km

RESULTS

In total, over 10 billion grid points are evaluated and 616,942 solutions are found using approximately 950 hours of total computer time on Linux machines with 3066 MHz processors. Approximately 5% of the solutions, or 30,040, are found to be stable in a linear sense and have close approaches above Europa's radius. Of those, 19,383 are planar.

Planar Case

It is customary to parameterize RTBP solutions with the Jacobi constant because it is indeed an integral of motion. Accordingly, although the grid search is performed in the (x_0,y_0) space, the solutions are plotted in the (J,x_0) space. Figure 7 and Figure 9 give a global view of planar motion periodic solutions in the vicinity of Europa for up to N=16. Note, there are three levels of stability indicated in all of the following plots: linearly stable (ρ=1), mildly unstable ($1< \rho \leq 10$), and highly unstable ($\rho>10$). The highly unstable solutions have an instablililty metric ρ that can vary by 10 or more orders of magnitude. Subsurface solutions are calculated for up to 100 km below Europa's mean radius. By this approach it is easy to track the end of a family to a physical collision.

As expected, the simply periodic (N=1) families form the backbone for all solutions. Starting with the direct case, there are three simply periodic solutions. The nomenclature for the families varies in the literature and is not descriptive in general because there are too many families to describe. Here, descriptive names are introduced for the main simply periodic solutions. The Circle-Egg family begins as a direct circular grazing orbit around Europa near J=568.75 km^2/s^2 and slowly transitions into an egg shaped orbit with its base oriented towards Jupiter. This is equivalent to Brouke's H1 family and Robin and Markellos' g1 family. This family is stable for almost the entire region of interest becoming unstable just prior to impact. The family transitions from being dominated by a circular shape to an egg-shape near an extremum in x_0 around J=566.23 km^2/s^2. The evolution of this family is followed in Row 5 of Figure 8.

The Egg-Diamond family begins as a grazing egg-shaped orbit with its base away from Jupiter (J=566.18 km^2/s^2 , x_0=11,500 km) and smoothly transitions to a circular-shape, then diamond-shape, and finally ends with two loops at the top and bottom of the diamond before colliding with the surface. This family is equivalent to Broucke's H2 family and Robin and Markellos' g2 family. From Figure 7, the family is stable for most of the egg-shaped portion until its maximum J value near 566.215. km^2/s^2. The solutions for decreasing values of J move rapidly towards instability. The evolution of this family is given in Row 4 of Figure 8.

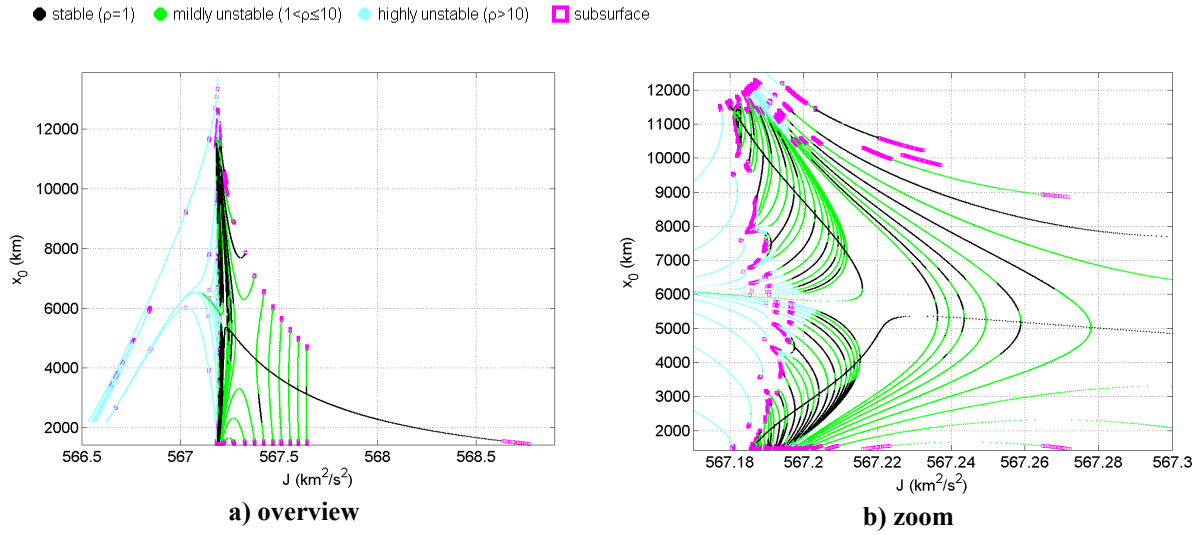

Figure 7: Planar direct solutions (N_{max}=16)

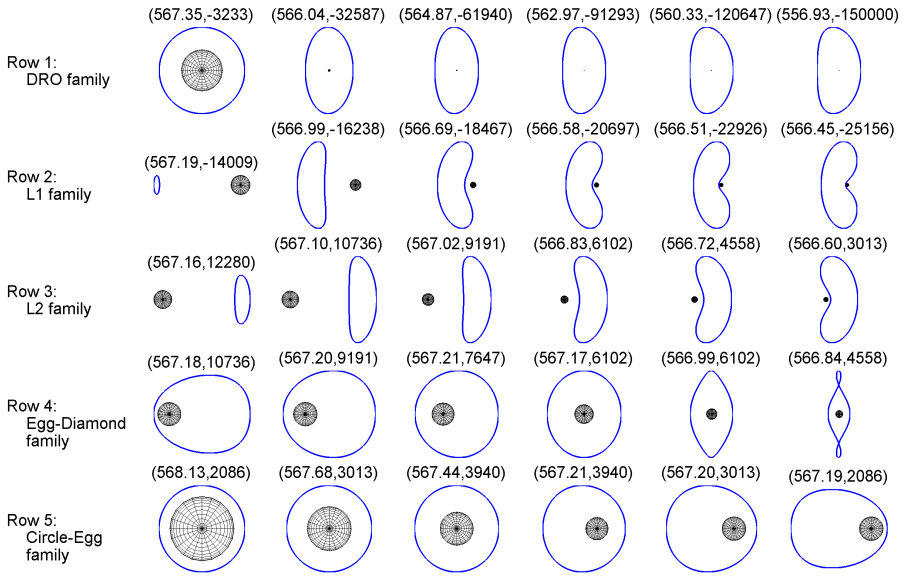

Figure 8: Evolution of the five simple periodic (N=1) planar families. Coordinates are associated with Figure 7 and Figure 9 and given in J (km^2/s^2) and x_0 (km).

It is noted that Henon's g and g' family in the Hill's model intersect whereas Figure 7(b) shows a clear gap between the Circle-Egg and the Diamond-Circle families.[3] In fact, by the current nomenclature, Henon's g' family is egg shaped on both ends, and the g family transitions from a circle to the diamond shapes, opposite from what is seen in the RTBP. Further investigation of this phenomenon is left to future work. To simplify discussion, however, the regions will be discussed in terms of branches: the circular-branch, the lower egg-branch (both of the Circle-Egg family), the upper egg-branch, and the diamond-branch (both of the Egg-Diamond family).

The third and final direct simple period family is the *L*2 family. This consists of closed orbits around the collinear libration point on the far side of Europa with respect to Jupiter. This family, unstable in its entirety, is shown as the top left most curve in Figure 7(a). It is noted that the curves on the bottom-left of Figure 7(a) indeed end with an impact, but the search failed to find these solutions because the escape condition was defined too liberally. The *L*1 family is analogous to the *L*2 family except of course it originates at the interior collinear libration point. This family is part of the bottom-right most curves given in Figure 9(c). The highly unstable top-left most families in Figure 9(c) are multiple-period and non-continuously orbiting (i.e. consecutive crossings of the *xz*-plane are not necessarily on opposite sides of Europa) families with properties of both the *L*1 and diamond orbits. The *L*1 and *L*2 simple period families are illustrated in rows 2 and 3 respectively of Figure 8.

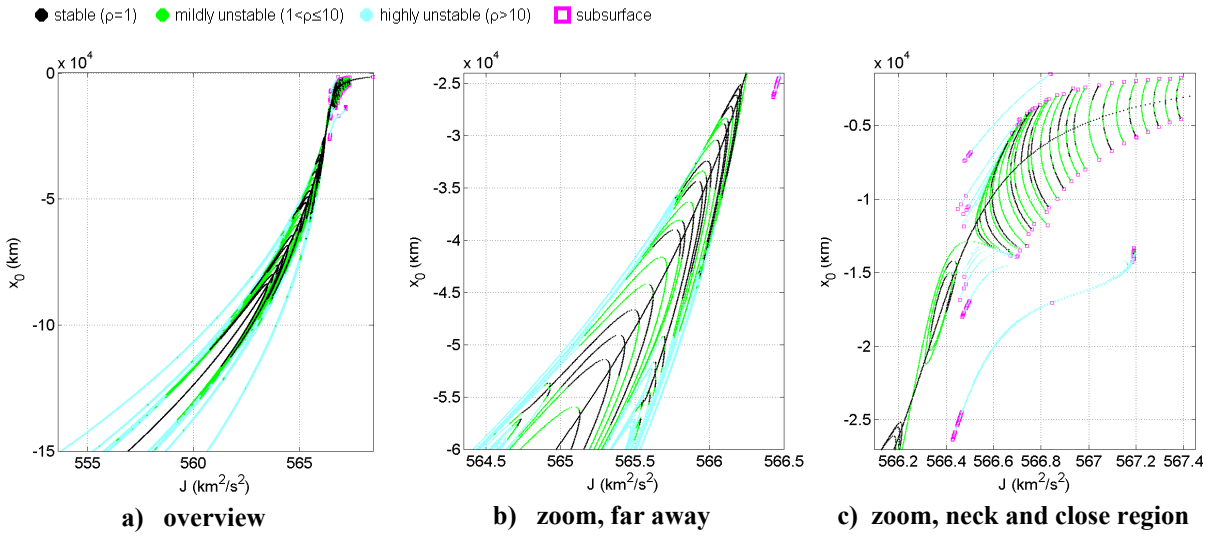

a) overview **b) zoom, far away** **c) zoom, neck and close region**

Figure 9: Planar retrograde solutions. Motion is centered around the stable DRO family.

The DRO (Distant Retrograde Orbit)[24] family begins as a grazing retrograde circular orbit and slowly transitions to a vertically aligned near-ellipse. The family continues to exist for increasing distances from Europa, and is remarkably stable to well beyond 150,000 km. From Figure 9, the DRO family is the stable curve that forms the central backbone for planar retrograde motion. The evolution of the simple period DRO family is illustrated in row 1 of Figure 8. The DRO is analogous to Broucke's family *C* and Henon's and Robin and Markellos' family *f*. Figure 9(b and c) illustrates the three distinct regions of motion near the DRO. Clearly inside approximately 13,000 km, the bifurcated families are oriented with a minima in *J*, while beyond approximately 25,000 km, the bifurcated families achieve a maxima in *J* at the intersection. In between these two points is commonly referred to as the "neck" of the DRO. Accordingly, the stability region around the neck shrinks in the planar case as indicated in Figure 9(c) by the lack of neighboring families at the neck's beginning and end.[17] Closer inspection reveals the boundaries are marked (and possibly enforced) by the intersection of the DRO curve with the associated N=3 curve. The stability region opens beyond the neck and remains intact for remarkable distances from Europa, making this an attractive region to investigate in the third dimension. Note the absence of intersecting families near and far away from Europa can be reduced by increasing N_{max}. This effectively fills in stable regions with stable and near-stable periodic orbits of higher resonance and fills the chaotic regions with highly unstable periodic orbits of higher resonance. This principle is valid for all of the presented results.

The families that surround the five planar simply periodic solutions in general are similar to their originating curves, but exist at a different resonances with respect to Europa's revolution around Jupiter. For example, the trajectory that bifurcates horizontally from an egg shaped orbit will appear similar to the top view

of the orbits shown in the Appendix in Figure 14(s) and Figure 15(d) among others. Orbits bifurcating horizontally from DROs will appear similar to the top views of the orbits shown in Figure 14(a-f) for example. Orbits bifurcating from the circular-branch such as those on the right side of Figure 7(b) appear similar to the top views of the orbits in Figure 15(o and q-s). Many of the circular-branch solutions appear to have symmetry in the *yz*-plane, but in fact do not in a similar manner that the upper egg-branch solutions do not share exact symmetry with those from the bottom branch. The solutions that appear as near-vertical lines on the right side of Figure 7(a) are near-stable, high-resonance orbits that appear as bird nests in the RTBP frame. These are effectively 2-body perturbed ellipses around Europa with a migrating orientation primarily due to the rotating frame. The orbits have a similar appearance to the top view of the orbit illustrated in Figure 15(e).

The results of the grid search in the planar case provide a global view of the geometry of the main and bifurcated families along with general regions of stability. Figure 9 shows a well-defined "cliff" where the stability properties change from near-stable with pockets of stability to clearly unstable. The diamond-branch and the *L*2 family clearly dominate the unstable motion, while the two egg-branches, the circular-branch, and the saddle structure that appears on the circular-branch near J=567.3 km^2/s^2 dominate the stable and near-stable regions and provide meaningful boundaries to classify the behaviors of the emanating orbits. In the retrograde case, the stable regions are clearly centered around the DRO family where the neck seems to play a critical role in the size of the region. The simply-periodic solutions and the general regions of stability provide the necessary framework for the discussion of the three-dimensional case.

Three-Dimensional Case

The addition of the third dimension brings added burden not only to the computational and algorithmic effort, but it also presents a new set of challenges associated with visualizing and interpreting the overwhelming number of resulting orbits and associated properties. The adopted strategy is first to present the results in a 3D volume view of the associated initial conditions. Then, each vector of initial conditions is represented in an alternate frame consisting of a proposed inclination angle that gives added insight and can be plotted against the x_0 axis crossing for a 2D view that captures the general essence of the associated 3D space.

The families of 3D periodic orbits are known to exist as lines through the (x_0, v_0, w_0) space. Again, similar to the planar case, the Jacobi constant is included in the parameterization and the results are presented in (x_0, J, w_0) where v_0 is easily recovered using Eq. (2). To emphasize the notion that most 3D solutions have a bifurcation history connecting them to the planar case, the planar solutions are included in the 3D views.

Figure 10 presents several views of the same set of the direct 3D solutions. Immediately, the apparent clustering of stable and near-stable solutions apart from the highly unstable solutions is evidence that boundaries of stability do indeed exist in the 3D case similar to those of the planar case. It is also clear at first glance that most solutions bifurcate from the planar case as expected. Figure 10(a) gives the appearance of a sitting swan. The neck and head of the swan in Figure 10(a) are clearly related to the unstable regions of diamond-branch and the L2 family from the planar case. The tail or the side of the body facing the viewer is clearly full of near-stable motion with many pockets of linearly stable solutions.

Surprisingly most of the 3D solutions are found to exist to the left of energies associated with the middle of the saddle structure that is observed in the planar case. This saddle is centered on the circular branch near J=567.3 km^2/s^2 This saddle is most clearly seen towards the lower right of Figure 10(b). Solutions to the right of the saddle do exist as evidenced by the peppering of solutions on the left side of Figure 10(a) and the right side of (b). These families bifurcate from the main circular-branch, and (b) indicates they generally start stable in the plane then transition to instability at some critical inclination. This is consistent with the results from Ref. 17. From (b) and (c) it is inferred that a large pocket of stable or near stable out-of-plane motion exists around 6000 to 8000 km with energy levels between 567 and 567.2 km^2/s^2. Note, this is directly above the planar, highly unstable region.

The vast majority of the solutions found in the 3D case bifurcate directly from the generally small region of planar solutions illustrated in Figure 7(b). From Figure 10(d), it is apparent that the general flow of the families is from either above or below the circular-branch away from the plane and towards a central stability region. In fact, many of the families bridge the gap entirely with the 3D motion by starting and ending on opposite sides of the circular-branch. For example, the lower right of Figure 10(b) shows clearly one continuous family that vertically bridges the two closest opposing saddle curves in the planar case.

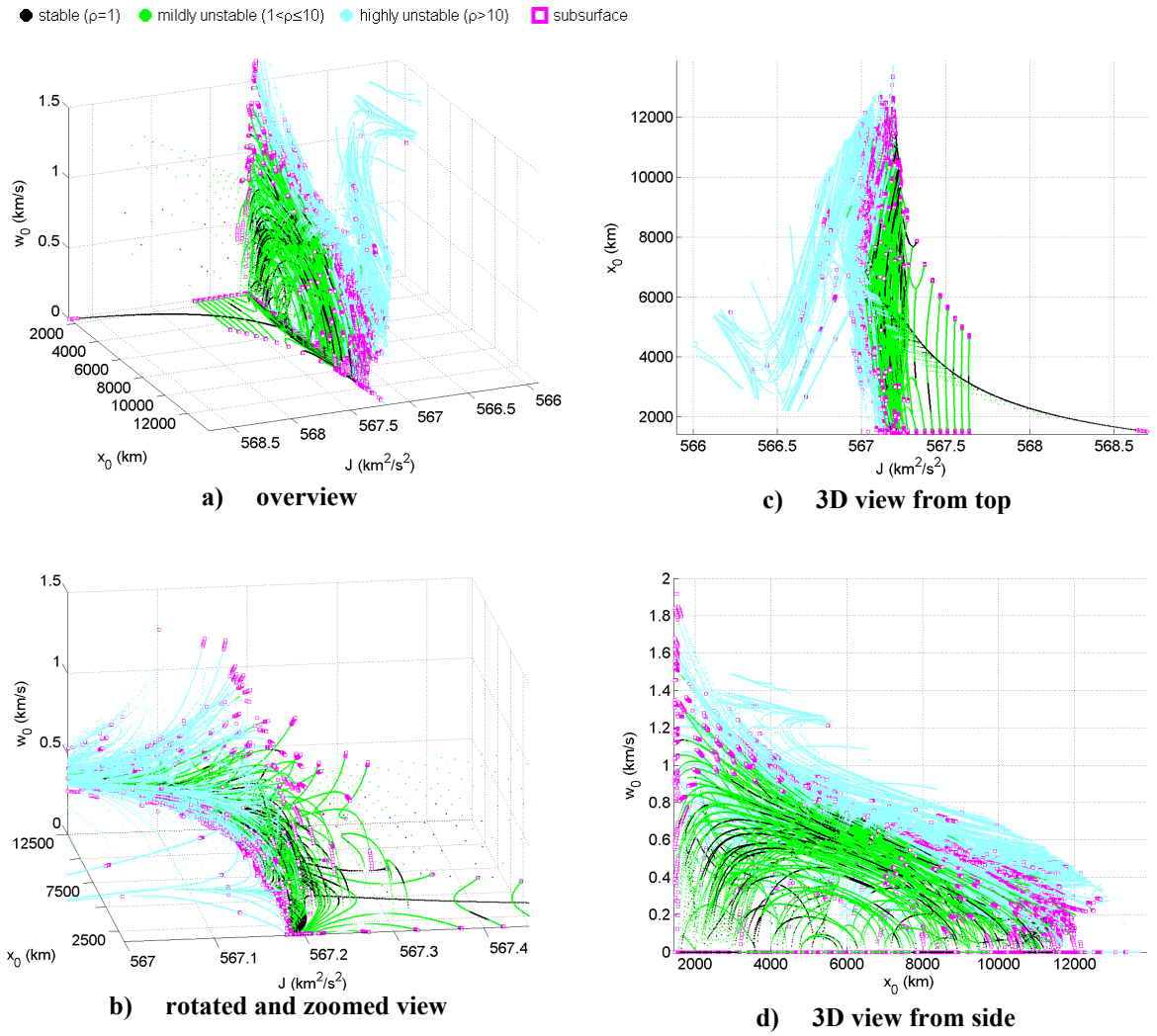

Figure 10: Direct 3D and planar solutions combined, 3D view.

Because many science missions require inclined orbits for mapping or other purposes, a pseudo inclination, i, is introduced and defined simply to be the out-of-plane angle of the initial departure from the xy plane. This provides a general metric of the expected out-of-plane motion for a particular orbit. Figure 11(a) plots this value against x_0 for each of the solutions. Figure 12(a and b) gives more detailed views. Note, that these are 2D plots, and the solutions are stacked on top of one another in the order of subsurface, highly unstable, mildly unstable, and finally stable. The resulting picture is representative of the understanding based on Figure 10, but incomplete without Figure 10 because of the lost dimension. It re-emphasizes the notion that the solutions clearly bifurcate from the plane and flow towards a highly inclined central region. The seemingly remarkable result is the existence of a plethora of highly (*pseudo*) inclined stable orbits.

Further investigation of the individual solutions that make up Figure 11(a) reveals that most of the stable solutions are of three general flavors, each corresponding to one of the three stable simple periodic planar branches shown in Figure 7. In general each of the stable solutions has qualities that are associated with either the circular-branch [Figure 15(s) for example] or one of the two egg-branches [Figure 14(v) or Figure 15(p) respectively]. As all three types approach the pinnacle of the stability region (around 7000 km and 70°) they move towards a highly inclined near-circular orbit with less distinguishable characteristics. The more circular orbits exist on and near the central ridge that runs vertically through the top of the stability region. This ridge is seen most clearly in Figure 12(b). Representative orbits near this feature include those presented in Figure 15(f-l). In general, the wavy families and the families with minima in inclination are related to the egg-branches, while the smoother more well behaved solutions, such as those that dominate the left side of Figure 11(a), are related to the circular-branch.

Note, there is one isolated stable solution that appears as a small speck in Figure 11(a) at x_0=11,034 km and i=86.7°. This somewhat pathological trajectory is plotted in Figure 15(u). Referred to as the "squid orbit" because of the top-down view, this orbit surprisingly meets the stability condition, and indeed is stable enough to withstand numerical integration for thousands of periods. However, when perturbing the initial position or velocity slightly, the trajectory quickly escapes indicating the stability island surrounding this orbit is very small.

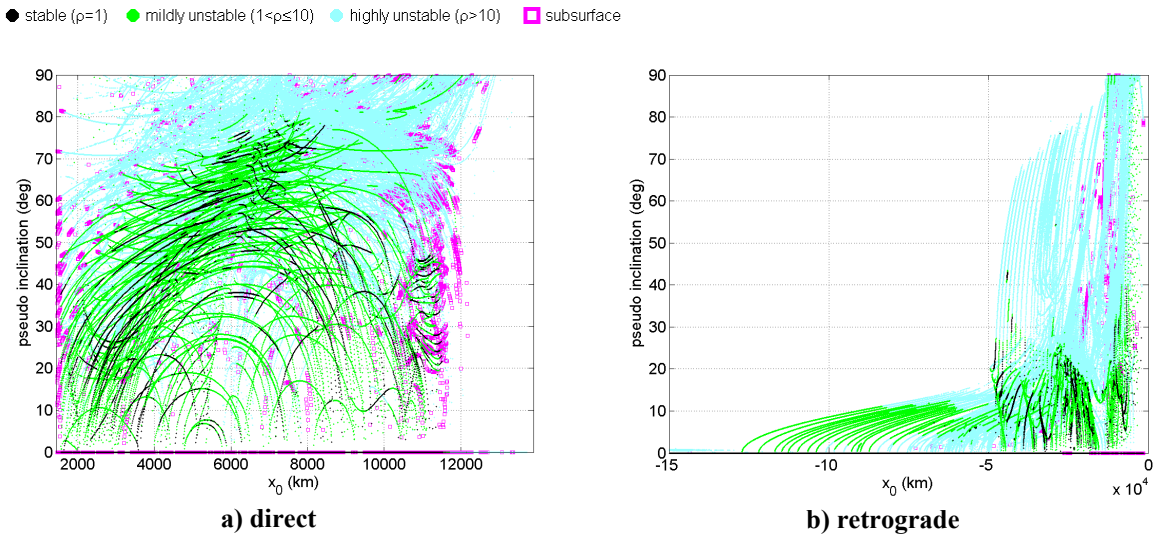

a) direct **b) retrograde**

Figure 11: Pseudo inclination vs. x_0 , Overview

The retrograde case appears much less complex than the direct case. The inclination overview is given in Figure 11(b) with more detailed views in Figure 12(c and d). The 3D volume views are given in Figure 13. Overall, the stable motion tends to stay closer to the plane than that of the direct case, and the flow of the more stable families is generally vertical with the clear exception being the 3D families very far away that move almost parallel to the plane in the direction of Europa. The vertical seeking families seen best in Figure 12(c) cease to exist for N_{max}≤16 beyond roughly 50,000 km. In general these families start stable and eventually switch to high instability at a critical inclination near 25° but may pass through the linear stability regions one or more times prior to the final switch. This is in general agreement with the "Red Sea" plot from Ref. 24. Also, the change in behavior of the solutions and the general absence of stable solutions near $L1$ is also generally consistent with the "Red Sea" plot.

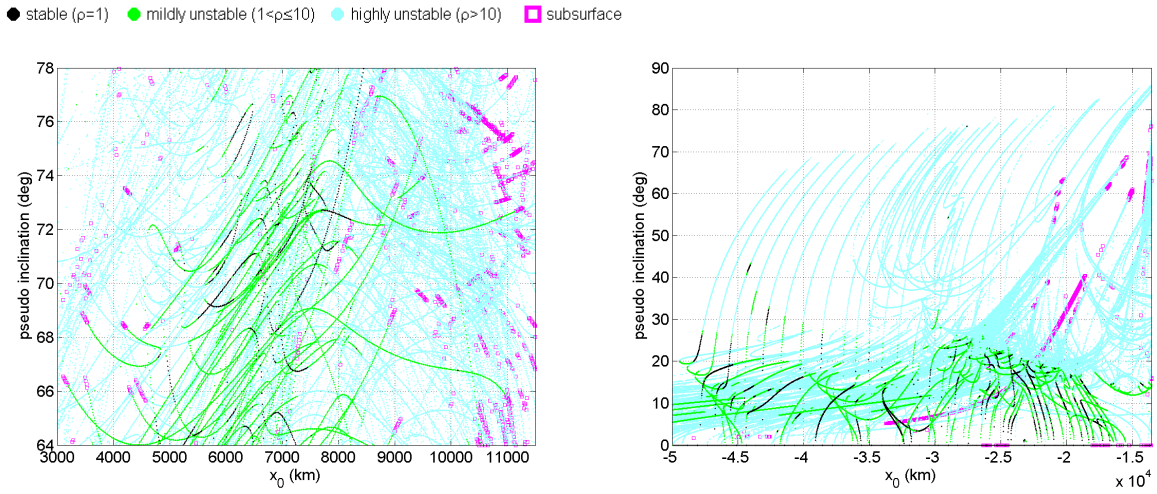

a) direct, zoom I. Some families appear to exist for the full x_0 span only at high inclinations. Orbits from Figure 15(k) and (r) are two stable solutions from such a family.

c) retrograde, zoom I. Note the absence of stable solutions near L1.

b) direct, zoom II. Central highly inclined stability region. The central ridge consists of the near-circular orbits.

d) retrograde, zoom II, inside *L*1.

Figure 12: Pseudo inclination vs. x_0 , Zoomed views

Note, the 3D solutions near -150,000 km begin at low inclinations and are similar to the DRO family, but have near collision flybys with Europa that generate large out-of-plane motion and accompanying instability. The solutions close to Europa that vertically bifurcate from the simple period DRO family appear as the sparse dots that rise almost exactly vertical from the plane in Figure 12(d). These solutions are infrequently spaced because of the high resonances associated with close periodic solutions.

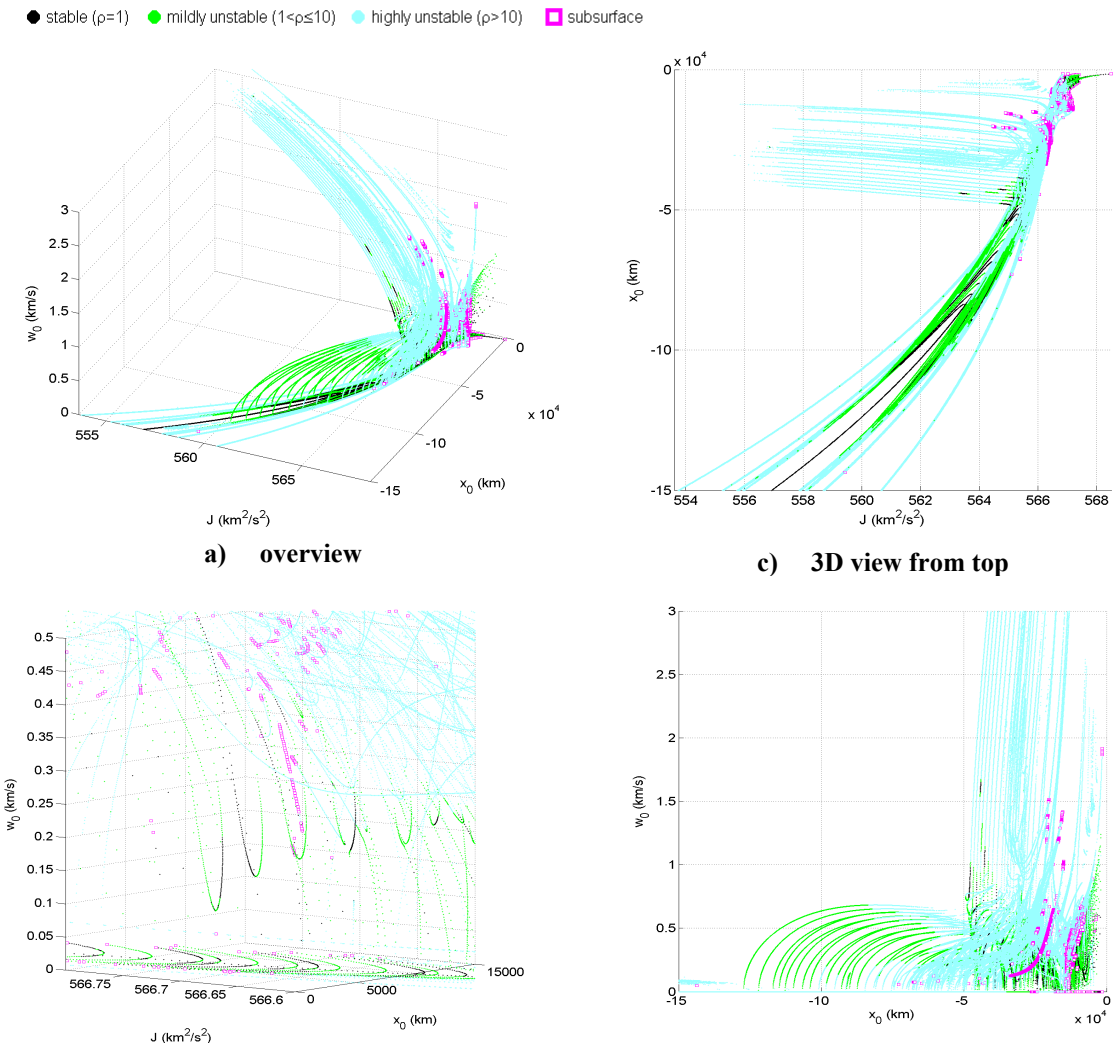

a) overview

c) 3D view from top

b) rotated and zoomed view close to Europa. Note the near stable highlighted solutions appear as loops in the left side of Figure 12(c).

d) 3D view from side

Figure 13: Volume views of the 3D and planar solutions combined

Similar to the direct case, the 3D solutions are generally related to the planar families as indicated by Figure 13(a and c). Isolated pockets of relatively high-inclined orbits with linear stability are noted from Figure 12(c) and Figure 13(c and d). These are documented in Figure 14(c,e,g, and h). It is quite remarkable that stable solutions exist at such distances (both in-plane and out-of-plane) from Europa. In the case of the orbits from Figure 14(c and e), the stability pockets appear to enjoy non-trivial radii as indicated by the multiple contiguous stable solutions as best seen in Figure 12(c) and Figure 13(d).

Figure 14(a-r) gives representative families of the set of found stable 3D retrograde orbits. For the retrograde case, the orbits generally take the shape of a cylindrical surface that maintains the shape of the DRO family of orbits when viewed from above. This is true despite the variety of behaviors from the different families of stable solutions seen in Figure 13 and Figure 12(c and d). Even the extreme case of the largely inclined orbit from Figure 14(h) partially maintains this general DRO shape when viewed from above. One exception where the cylinder form is clearly destroyed is the case of the axi-symmetric orbit illustrated in Figure 14(p).

The highly unstable orbits, both in the direct and retrograde cases have received much less attention and further analysis is left to future work. Figure 16 and Figure 17 are nonetheless included to give a general idea of the types of unstable solutions. Because approximately 95% of the found solutions are unstable, these figures are much less exhaustively representative of all the solutions. For simplicity, only highly-inclined low-resonance solutions are included, and they are ordered in increasing instability. These orbits are of general interest for manifold dynamics applications such as low energy captures or escapes from Europa. It is noted that orbits similar to those presented in Figure 16(b-h) have already been successfully applied to such applications, and the results are delayed to a future paper.

CONCLUSIONS

The conclusions fall into three general categories. First, an efficient means of globally identifying a complicated set of 3D periodic orbits near Europa is demonstrated. Differential correctors for axi- and doubly-symmetric orbits are derived and a grid search algorithm is proposed with modifications to existing techniques. The main contribution is the application of the grid search method to the Jupiter-Europa system and the previously unapproachable scale of the search due to the extraordinary speed of modern computers. The approach proves efficient in finding complicated intersections of families of periodic orbits, even those of high resonances, in a global manner without a priori information. It is noted that differential correcting and predicting to follow specific families of solutions is clearly still an invaluable tool for detailed analysis; the grid search is only emphasized as an efficient means for finding solutions on a global scale, and thus improving the preliminary view of the global solution space.

Secondly, the axi- and doubly-symmetric periodic orbits near Europa are analyzed in the planar and 3D case capturing a global view of the main solutions along with the flow of the accompanying higher order resonant solutions. Similar curves to those presented in this study have been previously published for other mass ratios and for small isolated values of N, but the full picture with the higher order resonances has received less attention. The visualization of all the higher order solutions together facilitates the identification of boundaries in phase space that separate regions of stability and mild instability with regions of chaos and strong instability. Several such boundaries are identified in all four cases: the planar direct, planar retrograde, 3D direct, and 3D retrograde. One of the fundamental results is the relative abundance of highly inclined direct 3D stable orbits compared to the retrograde side at similar distances to Europa. This is in clear opposition to the general attitude of mission planners that retrograde orbits are always more stable, presumably because of the impressively stable planar DRO family.

Lastly the resulting orbits of the study are of great practical use for preliminary design of missions to Europa.* The more stable solutions have obvious applications such as parking orbits, science orbits, and intermediate transfer orbits, while many of the unstable solutions are ideal for transfer applications using manifold dynamics. Each of the documented solutions (over 600,000) is associated with a list of defining characteristics including initial conditions, period, stability indices, type of symmetry, number of xz-plane crossings, minimum/maximum altitudes, and any other quantity that exists or can be defined in order to group or differentiate specific solutions. The final set is archived in an electronic text file and can be queried or sorted in a customized manner for a variety of potential Europa mission planning applications.

ACKNOWLEDGEMENTS

I wish to acknowledge Benjamin Villac, Try Lam, Martin Lara, Anastassios Petropoulos, Scott Zimmer, Jon Sims, and Jennie Johannesen for their interest in the study and for a variety of contributing discussions. The research described in this paper was carried out at the Jet Propulsion Laboratory, California Institute of Technology, under a contract with the National Aeronautics and Space Administration.

* Note, the solutions are generally scalable to be almost-valid for any RTBP system with a small mass ratio using the ratio of the corresponding $L1$ distances. Of course, if Hill's model were initially used, the solutions would be equally valid for all systems with small mass ratios. However, regions of interest in this study extend well beyond the range where Hill's model is appropriate.

APPENDIX

Selected periodic orbits are given in Figure 14- Figure 17 and accompanying data in Table 3.

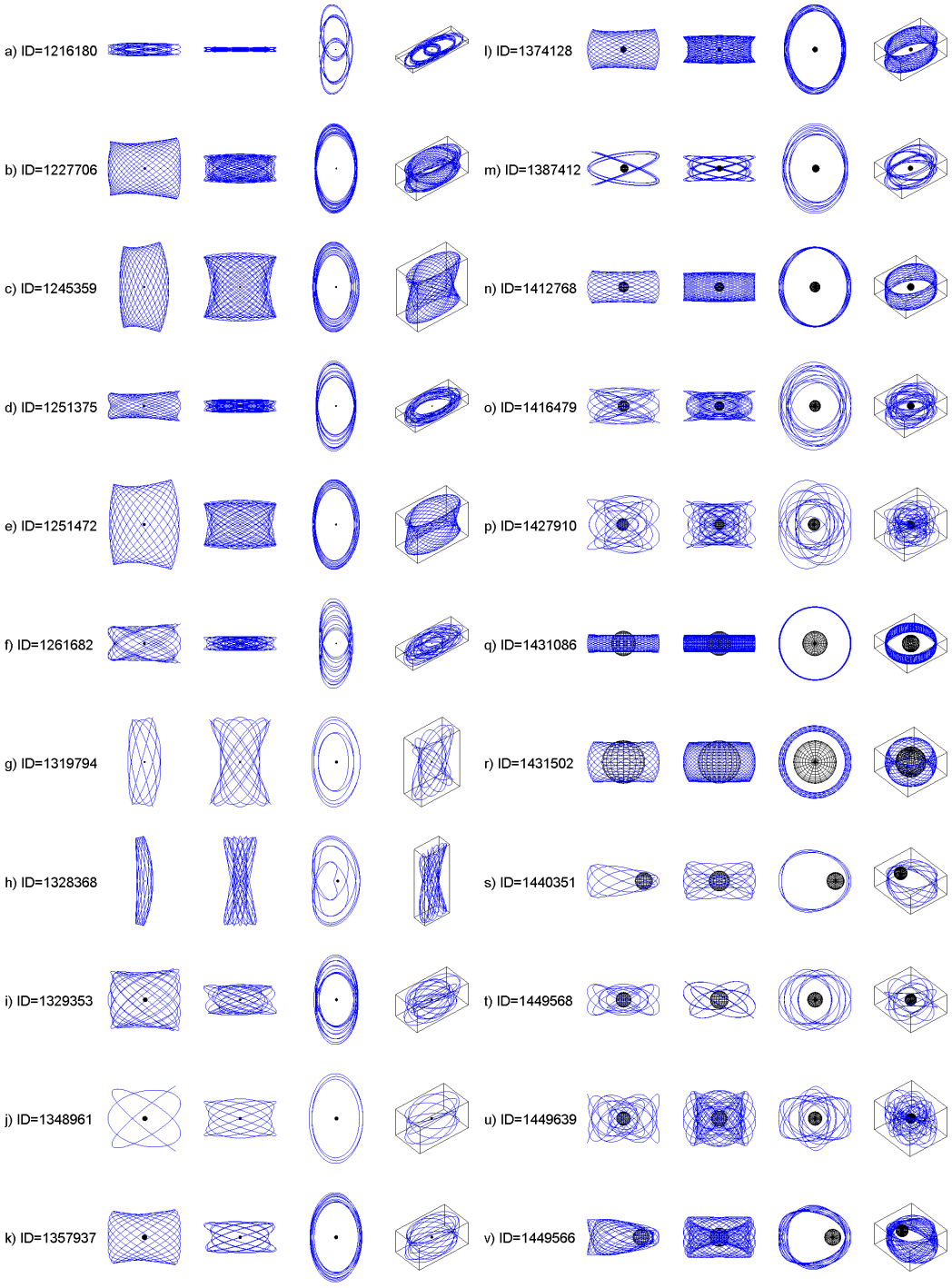

Figure 14: Representative set of 3D *stable* periodic orbits around Europa. *Part I*. Each orbit is illustrated from 4 viewing angles. From left to right: viewed from 1) negative *y* axis, 2) positive *x*-axis, 3) positive *z* axis, 4) azimuth=-130°, elevation=40°. Orbits are ordered in increasing x_0.

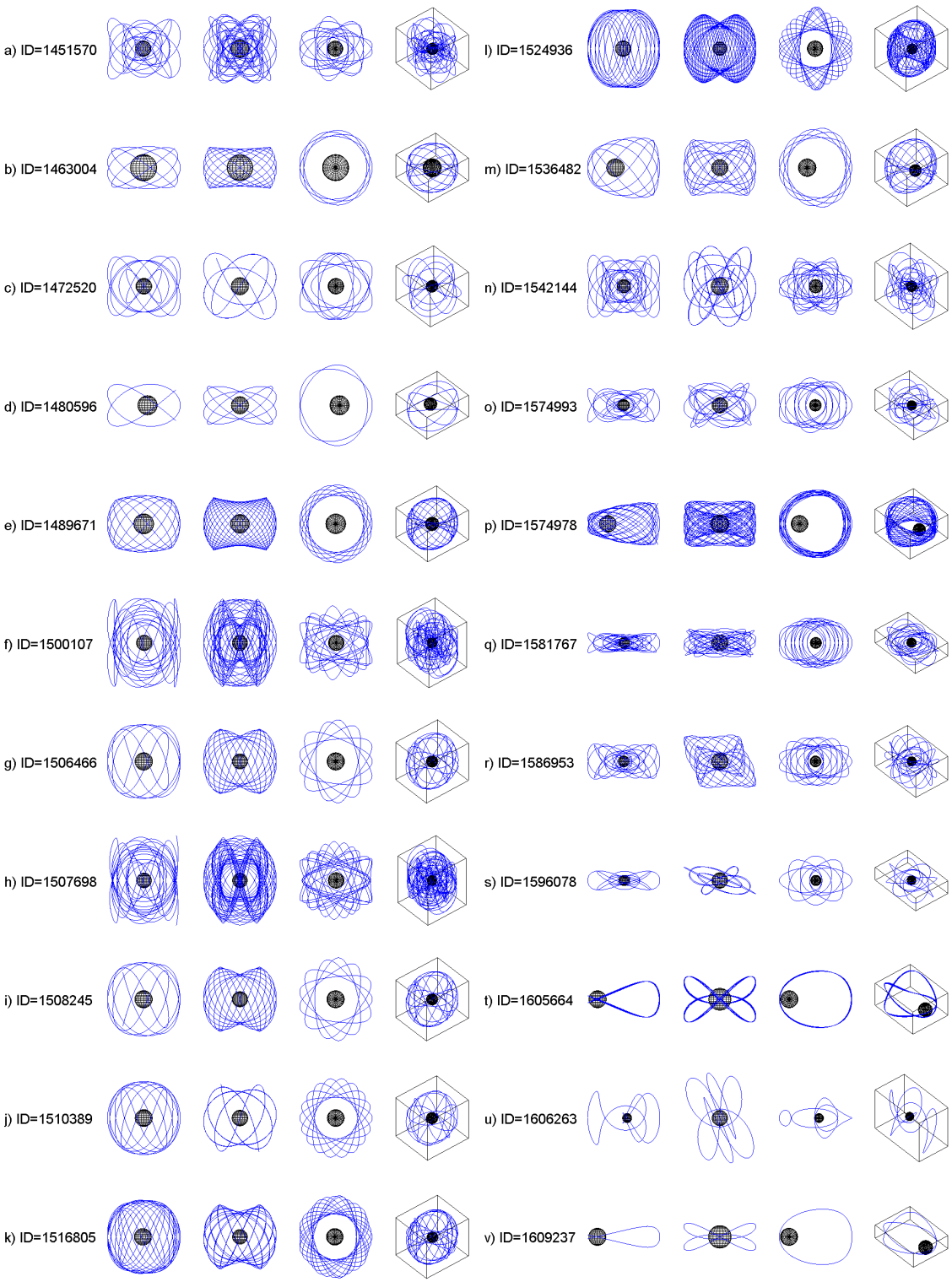

Figure 15: Representative set of 3D *stable* periodic orbits around Europa. *Part I*. Each orbit is illustrated from 4 viewing angles. From left to right: viewed from 1) negative *y* axis, 2) positive *x*-axis, 3) positive *z* axis, 4) azimuth=-130°, elevation=40°. Orbits are ordered in increasing x_0.

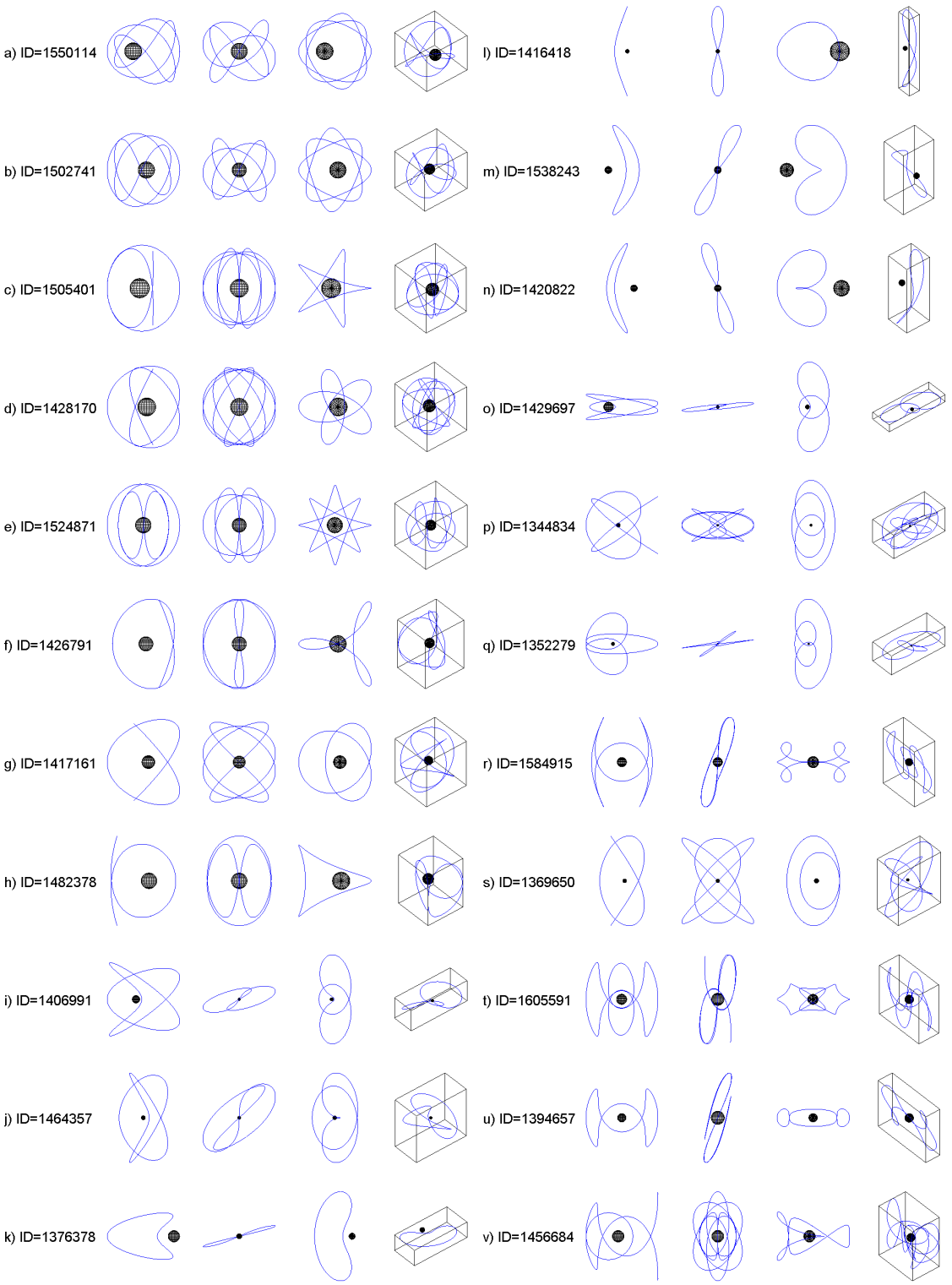

Figure 16: Representative set of 3D *unstable* periodic orbits around Europa. *Part I*. Each orbit is illustrated from 4 viewing angles. From left to right: viewed from 1) negative *y* axis, 2) positive *x*-axis, 3) positive *z* axis, 4) azimuth=-130°, elevation=40°. Orbits are ordered in increasing instability.

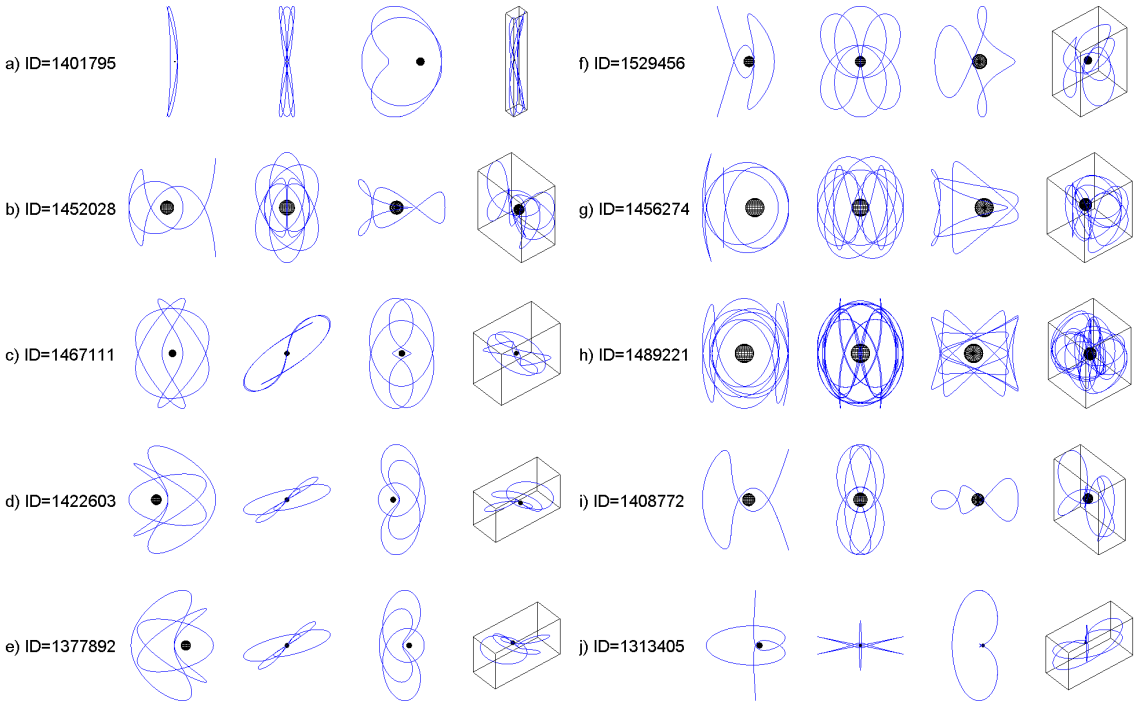

Figure 17: Representative set of 3D *unstable* periodic orbits around Europa. *Part II*. Each orbit is illustrated from 4 viewing angles. From left to right: viewed from 1) negative *y* axis, 2) positive *x*-axis, 3) positive *z* axis, 4) azimuth=-130°, elevation=40°. Orbits are ordered in increasing instability.

Table 3: Data for representative 3D orbits illustrated in Figure 14-Figure 17

ID	*N*	x_0 (km)	v_0 (km/s)	w_0 (km/s)	*T* (days)	sym[a]	*J* (km^2/s^2)	inc.[b] (deg)	h_{min}[c] (km)	k_1[d]	k_2[d]	ρ[d]
1216180	15	-5.38888889E4	2.20016215	0.23241350	9.91361806E1	D	565.579	6.0	2.42E4	7.53E-1	-1.74E0	1
1227706	16	-4.83708054E4	2.02455647	0.73731430	1.08864020E2	D	565.075	20.0	4.56E4	-1.74E0	-2.00E0	1
1245359	14	-4.42652349E4	1.78351364	1.57417442	9.52268856E1	D	563.555	41.4	4.27E4	-1.07E0	-2.00E0	1
1251375	13	-4.27989597E4	1.83726468	0.33348899	8.72318410E1	D	565.560	10.3	4.08E4	-1.93E0	-2.00E0	1
1251472	12	-4.27826678E4	1.77688902	1.03701719	8.07451033E1	D	564.813	30.3	4.12E4	1.20E0	-2.00E0	1
1261682	13	-4.03551678E4	1.75115279	0.49798404	8.70214382E1	D	565.469	15.9	3.42E4	-1.56E0	-1.65E0	1
1319794	5	-2.89996812E4	1.14109433	1.59105726	3.15533851E1	D	563.965	54.4	2.59E4	1.30E-1	-1.93E0	1
1328368	7	-2.75822819E4	0.79326209	3.19546760	4.60257067E1	D	556.864	76.1	2.23E4	-2.36E-1	-5.47E-1	1
1329353	14	-2.74030705E4	1.19161155	0.45551095	3.95055903E1	S	566.066	20.9	2.22E4	8.49E-1	-1.39E0	1
1348961	3	-2.43890604E4	1.09970988	0.42928366	1.62064532E1	D	566.124	21.3	2.28E4	-1.11E0	-1.86E0	1
1357937	11	-2.28413255E4	1.05637236	0.35406749	2.83892476E1	S	566.199	18.5	2.11E4	1.69E0	-1.98E0	1
1374128	15	-1.88497987E4	0.93533819	0.25374370	6.34213758E1	D	566.344	15.2	1.70E4	1.14E0	-2.00E0	1
1387412	10	-1.43695134E4	0.82273252	0.21717565	3.01875505E1	D	566.473	14.8	1.11E4	-5.82E-1	-1.33E0	1
1412768	11	-1.09644966E4	0.78186509	0.22057707	2.49854049E1	D	566.565	15.8	9.16E3	4.06E-1	-2.00E0	1
1416479	13	-1.00521477E4	0.73042229	0.25756442	2.31248108E1	D	566.653	19.4	4.97E3	-1.78E0	-1.97E0	1
1427910	15	-6.90780201E3	0.66816745	0.52088088	2.19708850E1	D	566.757	37.9	6.33E2	3.50E-2	-1.73E0	1
1431086	16	-4.57805369E3	0.91664623	0.19292502	1.16287865E1	D	567.036	11.9	3.02E3	1.04E0	-2.00E0	1
1431502	11	-2.63931208E3	0.98198381	0.59816765	3.66411901E0	D	567.601	31.3	1.08E3	-1.98E0	-2.00E0	1
1440351	4	2.80661224E3	1.15769161	0.51731633	7.95973106E0	D	567.172	24.1	5.94E2	-8.68E-1	-1.96E0	1
1449568	9	3.51004082E3	0.89312066	0.57479361	6.26782759E0	S	567.200	32.8	1.95E3	-1.99E0	-1.99E0	1
1449639	13	3.51004082E3	0.68382762	0.85141010	2.12323776E1	D	567.135	51.2	1.60E3	1.98E0	-1.90E0	1
1449566	15	3.51004082E3	0.94827283	0.51570043	2.97760253E1	D	567.163	28.5	7.72E2	4.97E-1	-1.94E0	1
1451570	12	3.63565306E3	0.52686236	0.90435700	1.53448697E1	D	567.170	59.8	1.68E1	-1.77E0	-1.99E0	1
1463004	4	4.32652041E3	0.63233404	0.49118888	3.34340758E0	D	567.350	37.8	2.76E3	-9.15E-1	-2.00E0	1
1472520	7	4.84153061E3	0.47178282	0.72636967	6.35999329E0	S	567.090	57.0	3.05E3	-1.15E0	-1.23E0	1
1480596	2	5.25605102E3	0.61615530	0.45236343	3.21078235E0	D	567.156	36.3	3.55E3	-1.44E0	-1.99E0	1
1489671	7	5.68313265E3	0.43451902	0.55331736	9.87662356E0	D	567.160	51.9	4.06E3	-2.00E0	-2.00E0	1
1500107	13	6.17302041E3	0.19939772	0.72537174	2.78513050E1	D	567.007	74.6	2.27E3	-1.46E0	-1.68E0	1
1506466	5	6.46192857E3	0.25910759	0.65136063	9.93223453E0	D	567.040	68.3	4.24E3	-4.65E-1	-1.99E0	1
1507698	16	6.51217347E3	0.18620979	0.69810413	3.46549601E1	D	567.002	75.1	2.36E3	-4.37E-1	-9.26E-1	1
1508245	5	6.53729592E3	0.25898815	0.64274970	9.93580189E0	D	567.041	68.1	4.42E3	-1.45E-2	-1.98E0	1
1510389	7	6.62522449E3	0.22764513	0.64215903	6.65127933E0	S	567.045	70.5	4.84E3	1.98E0	-2.00E0	1
1516805	13	6.90157143E3	0.24526771	0.61488819	1.32368170E1	S	567.037	68.3	4.63E3	-1.98E0	-2.00E0	1
1524936	13	7.24072449E3	0.16093253	0.65095131	2.99916208E1	D	566.988	76.1	3.95E3	4.39E-1	-1.95E0	1
1536482	5	7.79341837E3	0.30569385	0.43479349	9.42502216E0	D	567.103	54.9	2.85E3	-1.19E0	-1.97E0	1
1542144	15	8.10744898E3	0.13522813	0.48379377	1.20042117E1	S	567.107	74.4	5.26E2	1.24E0	-1.76E0	1
1574993	10	9.60223469E3	0.19574278	0.28856133	8.85300281E0	S	567.148	55.8	1.06E3	1.53E0	-1.62E0	1
1574978	14	9.60223469E3	0.22971910	0.25352166	2.60567868E1	D	567.152	47.8	1.28E3	1.08E0	-1.91E0	1
1581767	14	9.90370408E3	0.21509958	0.17287166	1.17671228E1	S	567.180	38.8	4.93E2	5.76E-1	-9.13E-1	1
1586953	13	1.01298061E4	0.12645618	0.29459818	1.13900048E1	S	567.145	66.8	7.64E2	-1.55E0	-1.82E0	1
1596078	7	1.05317653E4	0.11978504	0.16994878	5.58429568E0	S	567.191	54.8	3.07E2	-1.17E0	-1.56E0	1
1605664	16	1.10090918E4	0.17861206	0.17296747	1.94798048E1	S	567.158	44.1	2.06E2	-1.76E0	-2.00E0	1
1606263	4	1.10342143E4	0.02419184	0.42492975	4.73215069E0	S	567.038	86.7	6.49E2	1.83E0	-4.52E-1	1
1609237	1	1.12100714E4	0.17785598	0.09891667	2.41012034E0	D	567.174	29.1	2.13E2	1.76E0	-7.48E-1	1
1550114	6	8.49684694E3	0.23926555	0.43381321	6.11147444E0	S	567.086	61.1	2.52E3	-2.04E0	-3.27E0	2.93E0
1502741	3	6.29863265E3	0.31905840	0.64980487	3.27437882E0	S	567.030	63.8	4.27E3	-1.82E0	-3.50E0	3.19E0
1505401	2	6.41168367E3	0.01516162	0.72512880	3.43247503E0	D	567.012	88.8	4.77E3	-2.00E0	-1.10E1	1.10E1
1428170	3	-6.81005034E3	0.35668804	0.68175103	3.67123649E0	D	566.895	62.4	5.11E3	-2.00E0	-1.19E1	1.18E1
1524871	3	7.24072449E3	0.03137750	0.69425009	3.41027619E0	S	566.955	87.4	5.32E3	-1.81E0	-1.36E1	1.35E1
1426791	2	-7.26622483E3	0.15356112	0.76160114	3.45364150E0	D	566.832	78.6	5.71E3	-3.89E0	-3.67E1	3.67E1
1417161	2	-9.87293624E3	0.56390318	0.53604013	4.10426372E0	D	566.655	43.5	8.31E3	-3.55E0	-6.51E1	6.51E1
1482378	1	5.33141837E3	0.14029454	0.86662059	3.03142037E0	D	566.954	80.8	3.77E3	1.32E0	-1.24E2	1.24E2
1406991	2	-1.18442617E4	0.77642010	0.45940119	5.30691679E0	S	566.393	30.6	7.61E2	1.96E2	-2.30E1	1.96E2
1464357	2	4.38932653E3	0.00263312	1.40419427	6.42279922E0	S	565.999	89.9	2.83E3	-3.81E0	-2.66E2	2.66E2
1376378	1	-1.81655369E4	0.74387369	0.17620778	2.32440307E0	S	566.679	13.3	2.96E3	-2.09E0	-3.53E2	3.53E2
1416418	1	-1.00847315E4	0.30140764	1.02616364	3.03682020E0	D	566.108	73.6	8.52E3	-7.03E0	-3.99E2	3.99E2
1538243	1	7.88134694E3	0.07051949	0.88819045	2.40015997E0	S	566.584	85.5	6.32E3	-2.14E0	-4.08E2	4.08E2
1420822	2	-8.86283557E3	0.03174888	0.85205153	2.38083605E0	S	566.583	87.9	7.30E3	-2.06E0	-4.39E2	4.39E2
1429697	2	-6.02803691E3	0.99350835	0.22857417	3.99321009E0	S	566.557	13.0	6.74E2	4.83E2	-2.54E0	4.83E2
1344834	3	-2.50244463E4	1.06720556	0.59398454	1.61707067E1	D	566.060	29.1	1.28E4	-1.20E2	-6.82E2	6.82E2
1352279	3	-2.38677181E4	0.99780131	0.62452875	7.83794453E0	S	566.105	32.0	3.29E3	5.25E1	-1.49E3	1.49E3
1584915	3	1.00293163E4	0.01978593	0.66126393	4.52087233E0	S	566.814	88.3	4.72E3	-5.07E2	-3.02E3	3.02E3
1369650	2	-2.02346141E4	0.86977938	0.83967727	9.86919522E0	D	565.868	44.0	1.64E4	-7.53E1	-3.60E3	3.60E3
1605591	3	1.09965306E4	0.02136769	0.51863276	4.88201569E0	S	566.951	87.6	1.11E3	-4.18E0	-4.59E3	4.59E3
1394657	3	-1.31150336E4	0.18290585	0.42493343	4.12260170E0	S	566.981	66.7	4.48E3	-1.26E2	-1.11E4	1.11E4
1456684	3	3.94968367E3	0.01037729	1.07954634	7.16576896E0	D	566.963	89.4	2.39E3	-9.11E1	-3.61E4	3.61E4
1401795	2	-1.23493121E4	0.09452075	3.36673782	1.06121186E1	D	555.857	88.4	7.89E3	-1.88E3	-5.03E4	5.03E4
1452028	3	3.66077551E3	0.00908213	1.13212780	7.01340821E0	D	566.972	89.5	2.10E3	-3.41E1	-6.49E4	6.49E4
1467111	3	4.54006122E3	0.19929656	1.25464836	8.57965374E0	S	566.310	81.0	2.98E3	-2.64E2	-7.76E4	7.76E4
1422603	3	-8.42295302E3	0.78470294	0.45373928	6.91411796E0	S	566.516	30.0	1.98E3	8.03E4	-2.39E1	8.03E4
1377892	3	-1.76767785E4	0.72871009	0.46995860	7.08977522E0	S	566.498	32.8	2.15E3	8.07E4	-3.12E1	8.07E4
1529456	2	7.44170408E3	0.12962822	0.81496500	6.87744331E0	D	566.736	81.0	3.37E3	5.16E-1	-3.11E5	3.11E5
1456274	3	3.92456122E3	0.12204927	1.07198126	8.90492158E0	D	566.975	83.5	2.36E3	1.95E0	-3.49E5	3.49E5
1489221	6	5.65801020E3	0.16422706	0.81512762	1.57210818E1	D	566.968	78.6	3.78E3	1.01E-1	-4.25E5	4.25E5
1408772	3	-1.16650503E4	0.17156078	0.54422447	5.62437457E0	D	566.884	72.5	1.41E3	-2.34E0	-6.23E5	6.23E5
1313405	2	-3.00912416E4	1.23585853	0.24852279	1.04408738E1	D	566.286	11.4	5.32E2	-4.16E2	-6.38E6	6.38E6

[a] Doubly-symmetric (D) or Axi-symmetric (A) [b] pseudo inclination, range is between 0 and 90°, equal to $\tan^{-1}(w_0 / v_0)$ [c] close approach altitude

[d] for all cases presented the k_i values are non-complex. For stability, $|k_i| \leq 2$ or ρ=1. For unstable orbits, ρ is a scalar *in*stability metric.

REFERENCES

[1] Broucke, R., "Stability of Periodic Orbits in the Elliptic, Restricted Three-Body Problem," *AIAA Journal*, Vol. 7, No. 6, 1969, pp. 1003-1009.

[2] Broucke, R.A., "Periodic Orbits in the Restricted Three-Body Problem With Earth-Moon Masses", NASA-JPL TR 32-1168, Jet Propulsion Laboratory, Pasadena, CA, February 1968.

[3] Henon, M., "New Families of Periodic Orbits in Hill's Problem of Three Bodies," *Celestial Mechanics and Dynamical Astronomy*, Vol. 85, No. 3, 2003, pp. 223-246.

[4] Henon, M., "Numerical Exploration of the Restricted Problem. V. Hill's Case: Periodic Orbits and Their Stability", *Astronomy and Astrophysics*, Vol. 1, 1969, pp. 223-238.

[5] Henon, M., "Vertical Stability of Periodic Orbits in the Restricted Problem", *Astronomy and Astrophysics*, Vol. 30, 1974, pp. 317-321.

[6] Poincare, H., *New Methods of Celestial Mechanics, 1. Periodic and Asymptotic Solutions*, edited by F. Goroff, D. L., American Institute of Physics, USA, 1993.

[7] Szebehely, V., *Theory of Orbits. The Restricted Problem of Three Bodies*, Academic Press, New York, 1967. Section 8.6.3.

[8] Jefferys, W. H., "Doubly Symmetric Periodic Orbits in the Restricted Three-Body Problem," *The Astronomical Journal*, Vol. 70, No. 6, 1965, pp. 393-394.

[9] Jefferys, W. H., "Periodic Orbits in the Three-Dimensional Restricted Problem," *The Astronomical Journal*, Vol. 71, No. 7, 1966, pp. 566-567.

[10] Bray, T. A., Goudas, C. L., "Doubly Symmetric Orbits about the Collinear Lagrangian Points," *The Astronomical Journal*, Vol. 72, No. 2, 1967, pp. 202-213.

[11] Goudas, C. L., "Three-Dimensional Periodic Orbits and Their Stability," *Icarus*, Vol. 2, 1963, pp. 1-18.

[12] Zagouras, C., Markellos, V. V., "Axi-symmetric Periodic Orbits of the Restricted Problem in Three Dimensions," *Astronomy and Astrophysics*, Vol. 59, 1977, pp. 79-89.

[13] Papadakis, K. E., Zagouras, C. G., "Bifurcation Points and Intersections of Families of Periodic Orbits in the Three-Dimensional Restricted Three-Body Problem," *Astrophysics and Space Sciences*, Vol. 199, 1993, pp. 241-256.

[14] Robin, I. A., Markellos, V. V., "Numerical Determination of Three-dimensional Periodic Orbits Generated from Vertical Self-resonant Orbits," *Celestial Mechanics*, Vol. 21, 1980, pp. 395–434.

[15] Lara, M., and Scheeres, D.J., "Stability bounds for three-dimensional motion close to asteroids." *The Journal of the Astronautical Sciences*, Vol. 50, No. 4, 2002, pp. 389–409.

[16] Lara, M., and Pelaez, J., "On the numerical continuation of periodic orbits, An intrinsic, 3-dimensional, differential, predictor-corrector algorithm." *Astronomy and Astrophysics*, Vol. 389, 2002, pp. 692-701.

[17] Lara, M., Russell, R.P., Villac, B., "On Parking Solutions Around Europa", AAS paper 05-384, presented at the same conference.

[18] Kazantzis, P. G., Goudas, C. L., "A Grid Search For Three-Dimensional Motions and Three New Types of Such Motions," *Astrophysics and Space Sciences*, Vol. 32, 1975, pp. 95-113.

[19] *Jupiter, The Planet, Satellites, and Magnetosphere*, edited by F. Bagenal, T. Dowling, W. McKinnon, Cambridge Planetary Society, Cambridge, United Kingdom, 2004. pp. 36, 347.

[20] *Applied Nonlinear Dynamics*, Nayfeh, A. H., Balachandran, B., John Wiley and Sons, Inc., New York, 1995. Sec. 3.2.

[21] Battin, R. H., *An Introduction to the Mathematics and Methods of Astrodynamics*, American Institute of Aeronautics and Astronautics, Inc., New York, 1987, pg. 453.

[22] Ocampo, C. A., "Trajectory Optimization for Distant Earth Satellites and Satellite Constellations," Ph.D. Thesis, Department of Aerospace Engineering, University of Colorado, Oct. 1996. Sec. 2.5.

[23] Howell, K. "Three-dimensional, periodic halo orbits in the restricted three-body problem," Ph.D. Thesis, Department of Aeronautics & Astronautics, Stanford University, 1983.

[24] Lam, T., Whiffen, G.J., "Exploration of Distant Retrograde Orbits around Europa," Paper AAS 05-110, presented at the 15th Spaceflight Mechanics Meetings, Copper Mountain, Colorado, January 2005.